
Relative Advantages of Thin-Layer Navier-Stokes and Interactive Boundary-Layer Procedures

Unmeel Mehta, K.C. Chang, and Tuncer Cebeci

November 1985

LIBRARY COPY

DEC 12 1985

LANGLEY RESEARCH CENTER
LIBRARY, NASA
HAMPTON, VIRGINIA



National Aeronautics and
Space Administration



NF00041

Relative Advantages of Thin-Layer Navier-Stokes and Interactive Boundary-Layer Procedures

Unmeel Mehta, Ames Research Center, Moffett Field, California

K. C. Chang,

Tuncer Cebeci, Douglas Aircraft Co., Long Beach, California

November 1985



National Aeronautics and
Space Administration

Ames Research Center
Moffett Field California 94035

N86-15244 #

This Page Intentionally Left Blank

TABLE OF CONTENTS

SUMMARY	1
INTRODUCTION	1
THIN-LAYER NAVIER-STOKES METHOD	2
INTERACTIVE BOUNDARY-LAYER METHOD	3
TURBULENCE MODELS AND TRANSITION CRITERIA	4
Eddy-Viscosity Model $(\mu_t)_a$	4
Eddy-Viscosity Model $(\mu_t)_b$	6
Transition Criteria	8
Various Models	9
DISCUSSION OF RESULTS	9
Computational Grids	10
Transition Locations	11
Comparison of Loads	13
Some Flow-Field Details	17
Computational Efficiency	22
UPSTREAM INFLUENCES	24
CONCLUDING REMARKS	37
APPENDIX: THE TLNS METHOD	38
Linearization and Approximate Factorization	38
Numerical Dissipation	40
Spatial Differencing	41
Boundary Conditions	42
Numerical Solution Procedure	44
REFERENCES	46

RELATIVE ADVANTAGES OF THIN-LAYER NAVIER-STOKES AND INTERACTIVE BOUNDARY LAYER PROCEDURES*

SUMMARY

Numerical procedures for solving the thin-shear-layer Navier-Stokes equations and for the interaction of solutions to inviscid and boundary-layer equations are described and evaluated. To allow appraisal of the numerical and fluid dynamic abilities of the two schemes, they have been applied to one airfoil as a function of angle of attack at two slightly different Reynolds numbers. The NACA 0012 airfoil has been chosen because it allows comparison with measured lift, drag, and moment and with surface-pressure distributions. Calculations have been performed with algebraic eddy-viscosity formulations, and they include consideration of transition. The results are presented in a form that allows easy appraisal of the accuracy of both procedures and of the relative costs. The interactive procedure is computationally efficient but restrictive relative to the thin-layer Navier-Stokes procedure. The latter procedure does a better job of predicting drag than does the former. In both procedures, the location of transition is crucial for accurate or detailed computations, particularly at high angles of attack. When the upstream influence of pressure field through the shear layer is important, the thin-layer Navier-Stokes procedure has an edge over the interactive procedure.

INTRODUCTION

It is generally accepted that the Navier-Stokes equations correctly represent fluid-flow phenomena. Since the unsteady, three-dimensional equations can usually be solved for flows in which small-scale fluctuations are unimportant, emphasis has been placed on particular reduced forms such as those appropriate to regions of inviscid flow and boundary layers. In recent years, and with the application of numerical solution procedures in mind, attention has also been paid to the Reynolds-averaged Navier-Stokes equations and to various further-reduced forms, including their so-called parabolized forms and the thin-layer Navier-Stokes (TLNS) equations.

In this report, we are concerned with calculating the properties of steady incompressible flows around airfoils at angles of attack from 0° up to values where separation can occur near the trailing edge of the suction surface. The consideration of airfoils itself introduces a simplification in that the corresponding Reynolds-averaged equations have only two independent variables. Three main approaches to problems of this type are described in the literature and are characterized by

* This paper was presented at the Third Symposium on Numerical and Physical Aspects of Aerodynamic Flows, Jan , 1985

different forms of equations. The first possibility is to reduce the Navier-Stokes equations to a Reynolds-averaged, two-dimensional form resulting in elliptic equations that can be numerically solved. The second possibility is to further reduce the equations by neglecting the longitudinal diffusion terms leading to the TLNS equations, which are elliptic-parabolic and strongly coupled. The third possibility is to solve inviscid-flow equations and to use the resulting pressure distribution as a condition for the solution of the boundary-layer equations, which are parabolic, with or without a second momentum equation to represent any normal pressure gradient. This classic approach has been improved in recent years by interaction of the two solutions to ensure that the viscous flow is allowed to influence the inviscid flow and vice versa.

The design requirement that calculations be performed for several geometries and angles of attack and for the necessary extension to three dimensions, together with the present emphasis on flows with small or no separation, suggests that the choice of methods lies between those methods associated with interactive boundary layers (IBL) and those associated with TLNS equations. As a consequence, we have performed calculations with the IBL procedure of Cebeci et al. (ref. 1) and with the TLNS procedure developed at Ames Research Center (refs. 2-4). The results to date correspond to a NACA airfoil at several angles of attack. It is expected that these and similar results for a range of airfoils will permit the determination of a range of parameters for which one or the other method is preferable.

In this report, we present results that show the influence of transition location and of the turbulence model, in particular, models based on the Cebeci-Smith (ref. 5) and Baldwin-Lomax (ref. 2) eddy-viscosity formulations. The former formulation has been extensively used in previous boundary-layer calculations and the latter in previous applications of the TLNS equations. Since, in principle, the Baldwin-Lomax model does not apply to the far-wake region, the model developed by Chang et al. (ref. 6) has also been used for wake calculations.

The TLNS procedure and the IBL procedure are described in the following two sections, which are followed by a description of the turbulence models and transition criteria. Computed loads acting on a NACA 0012 airfoil are then compared with each other and with experimental data. In addition, some details of the flow field, in the form of pressure distributions and displacement-thickness distributions, are presented. The report ends with a discussion of upstream influences and concluding remarks.

The authors gratefully acknowledge the assistance provided by Dr. Thomas Pulliam in the use of the ARC2D code.

THIN-LAYER NAVIER-STOKES METHOD

Some viscous-flow problems can be represented by a set of equations that falls between the boundary-layer equations and the full Navier-Stokes equations. This intermediate set of equations is applicable to both inviscid and viscous regions, in common with the Navier-Stokes equations; therefore, it can be used to compute strong interactions between the two regions. Since they couple the viscous and inviscid approximations to a fluid flow, they have been referred to as composite equations (ref. 7). A main feature of these equations is the presence of a nonzero,

normal-pressure gradient, which is necessary to couple and solve simultaneously the viscous and inviscid regions. Relative to the Navier-Stokes equations, these composite equations require less computational effort because they contain fewer terms.

The composite, thin-layer equations are generally referred to in the literature as TLNS equations. They are obtained by neglecting all streamwise and spanwise derivatives of the viscous and turbulence stress, conductive heat-flux terms, and any term involving mixed derivatives. These approximations are justified either by physical order of magnitude analysis or by a computational accuracy argument which amounts to the observation that since the neglected terms cannot be computed correctly with the available grid resolution anyway, why keep them? The TLNS equations are primarily based on this latter argument, which is computational rather than physical.

The form of the TLNS equations generally used elsewhere and here, does not satisfy relationships between metric coefficients in diffusive and conduction terms (ref. 8). The error introduced by this oversight is usually insignificant, except when the effective viscosity is relatively large. Another limitation of these equations is that the longitudinal-curvature diffusive terms are neglected. This limitation is a consequence of using the Cartesian velocity components instead of curvilinear velocity components with curvilinear coordinates. This problem has been discussed in detail by Blottner (ref. 9).

An implicit numerical method is used to solve the TLNS equations. Some parts of this method are essentially those given by Beam and Warming (ref. 3). Other parts are from the numerical schemes presented by Steger (ref. 4), Pulliam and Chaussee (ref. 10), Salas et al. (ref. 11), and Jameson et al. (ref. 12) Since only steady-state computations are of interest, a diagonal form for the Euler equations and a spatially varying time-step are used. These different parts have been incorporated in the ARC2D computer code, which is a continuously evolving code. There is no detailed documentation of this code. The version 142 of ARC2D code (ARC2D142) was utilized with a few crucial modifications for the present study. (The parts of ARC2D142 that have been used here are identical to those in ARC2D150, which is the current version of this code.) The turbulence modeling modifications are identified in section 4, and the numerical modifications are incorporated in the numerical method presented in the appendix. This method is outlined for completeness and for documenting a novel derivation of the basic numerical scheme.

INTERACTIVE BOUNDARY-LAYER METHOD

The IBL method of Cebeci et al. (ref. 1) has as its essential components Halsey's inviscid procedure (ref. 13), based on the conformal mapping and Fourier analysis techniques, and an inverse finite-difference boundary-layer procedure due to Cebeci et al. (ref. 14) This method employs a viscous/inviscid iteration procedure in which viscous calculations are performed over the airfoil and wake. After each viscous sweep, the external inviscid solution is recomputed, and the whole cycle is repeated until a converged solution is obtained. The inverse boundary-layer code incorporates the eddy-viscosity formulation, and is able to compute flows with large regions of separation without numerical problems. In regions of reverse flow, it uses the FLARE approximation, in which the streamwise convective term is set equal to zero in the recirculating

region.

The boundary-layer calculation is initiated on each surface of the airfoil by a direct solution in which the boundary condition at the outer edge follows from matching the viscous velocity with the latest computed inviscid surface-velocity distribution. As the calculation proceeds downstream, the boundary-layer algorithm is switched into an inverse mode, in which the viscous-edge velocity is computed as part of the boundary-layer solution. This calculation is accomplished by applying an interaction procedure suggested by Veldman (ref. 15) and further developed by Cebeci et al. (ref. 1) and Cebeci et al. (ref. 14). An overrelaxation scheme is employed, and studies have shown that the rate of convergence is considerably improved when it is combined with the interactive viscous calculation. In addition, the solution for each successive angle employs the previous solution as the starting solution when calculations are required for a range of angles of attack. In this way, the converged solution for each angle of attack requires fewer than 10 iterations.

The method for calculating the wake region has some novel features which allow results to be obtained at high angles of attack. A sudden jump is introduced at the trailing edge by the removal of the no-slip boundary condition on the airfoil surface. To account for this jump, a small step, with the size related to chord Reynolds number, is employed in the immediate vicinity of the trailing edge. For wake calculations involving reverse-flow regions, an additional iterative scheme is employed with the FLARE approximation and is based on the homotopy continuation method. Studies by Cebeci et al. (ref. 1) have shown that without this added feature, the boundary-layer calculations would break down when significant trailing-edge separation region is present. Thus, the trailing-edge velocity profile is modified to correspond to an attached flow profile; it thereby allows boundary-layer calculations to be performed at the next downstream station. The upstream profiles are gradually modified and the downstream profile is recomputed until a solution is obtained for the original separated velocity profile. This computational scheme is employed at each wake station for which there is flow reversal. Further details are provided in reference 1.

TURBULENCE MODELS AND TRANSITION CRITERIA

Two algebraic, eddy-viscosity, turbulence models have been used in the present calculations. The first, $(\mu_t)_a$, is described by Cebeci et al. (ref. 1); the second, $(\mu_t)_b$, is based on the Baldwin-Lomax model (ref. 2). Both models stem from the earlier work of Cebeci and Smith (ref. 5). The particular formulations used here are described below.

Eddy-Viscosity Model $(\mu_t)_a$

A zero-equation turbulence model, used in the Reynolds-averaged formulation for wall-bounded flows that are steady, is due basically to Cebeci and Smith (ref. 5) and is discussed in some detail by Cebeci and Smith (ref. 16). The present version of this model is described by Cebeci et al. (ref. 1). This model is briefly outlined next. The model is extended into the wake region of the

airfoil as done by Chang et al. (ref. 6). This combination of the eddy-viscosity formulation in the boundary layer and the wake is labeled as model $(\mu_t)_a$. The nondimensional eddy viscosity is represented by

$$\mu_{tbl} = Re\rho\alpha v\ell\gamma_{tr}(\gamma_k)_a \quad (1)$$

In the inner layer, $0 \leq y \leq y_c$, the expressions for v and ℓ are

$$(v)_{inner} = \ell \left| \frac{\partial u}{\partial y} \right|, \quad (\ell)_{inner} = 0.4y \left[1 - \exp\left(-\frac{y^+}{26}\right) \right] \quad (2)$$

where, with w denoting conditions at the wall and max designating the maximum value in the boundary layer,

$$y^+ = y \left[\frac{Re\rho_w \left| \frac{\partial u}{\partial y} \right|_{max}}{\mu_w} \right]^{1/2}$$

The use of the maximum value of $|\partial u / \partial y|$, instead of the wall value, accounts for the effect of the pressure gradient. In the outer region, $y > y_c$, the expressions for v and ℓ , with the subscript e denoting the edge velocity and δ^* the usual definition of displacement thickness, are

$$(v)_{outer} = u_e, \quad (\ell)_{outer} = \delta^* \quad (3)$$

The distance y_c is defined by the continuity of the two eddy viscosities.

The value of α in the inner layer is 1.0, and its value in the outer layer, suggested by Simpson et al. (ref. 17), is

$$\alpha = \frac{0.0168}{F^{2.5}} \quad (4)$$

The parameter F is determined from

$$F = \left\{ 1 - \beta \left[\frac{(\partial u / \partial x)}{|\partial u / \partial y|} \right]_{\mu_{tbl} \partial u / \partial y|_{max}} \right\} \quad (5)$$

with the condition that

$$F = \begin{cases} 1.9919, & \text{if } F > 1.9919 \\ 0.5867, & \text{if } F < 0.5867 \end{cases}$$

The value of β depends on

$$R_T = \frac{(\mu \partial u / \partial y)_w}{(\mu_{tbl} \partial u / \partial y)_{max}} \quad (6)$$

and it is determined from the experimental data of Nakayama (ref. 18),

$$\beta = \begin{cases} (1 + R_T) / R_T, & \text{if } R_T \geq 1.0 \\ 6 / [1 + 2R_T(2 - R_T)], & \text{otherwise} \end{cases} \quad (7)$$

If $R_T < 0$, then R_T is taken to be zero.

In equation (1), γ_{tr} is a transition factor accounting for the transition region that exists between a laminar and turbulent flow. It is determined by

$$\gamma_{tr} = 1 - \exp \left[-G(x - x_{tr}) \int_{x_{tr}}^x \frac{dx}{u_e} \right] \quad (8)$$

where the empirical factor G is

$$G = \frac{Re^2 u_{e_{tr}}^3}{1200} (Re u_{e_{tr}} x_{tr})^{-1.34}$$

and where the subscript tr designates values at the beginning of transition.

Further, in equation (1), $(\gamma_k)_a$ is the Klebanoff intermittency factor, which accounts for intermittent (laminar-turbulent) nature of the outer part of the boundary layer; it is given by

$$(\gamma_k)_a = \left[1 + 5.5 \left(\frac{y}{\delta} \right)^6 \right]^{-1} \quad (9)$$

where δ is the boundary-layer thickness.

The airfoil wake is divided into two regions, the first of which is near the trailing edge and the second of which is farther away. In the near-wake, the flow is adjusting to the sudden elimination of the wall-boundary condition at the trailing edge, while asymptotically approaching the far-wake condition. Therefore, one would expect that the eddy viscosity would be close to that for the boundary layers at the trailing edge, and that it would asymptotically approach the far-wake expression. Based on the study dealing with wakes subjected to adverse pressure gradients by Chang et al. (ref. 6), this is accomplished with the expression

$$\mu_{tw} = \mu_{tf} + (\mu_{te} - \mu_{tf}) \exp \left(-\frac{x - x_{te}}{20\delta_{te}} \right) \quad (10)$$

where

$$\mu_{tf} = 0.064\rho\gamma_k \{ \text{maximum of } [(u_e\delta^*)_\ell, (u_e\delta^*)_u] \} \quad (11)$$

Here the subscripts ℓ and u denote the lower wake and the upper wake, respectively; and the displacement thickness is measured from the location of minimum velocity.

Eddy-Viscosity Model $(\mu_t)_b$

The second zero-equation model is patterned after that of Baldwin and Lomax (ref. 2). The Baldwin-Lomax model is patterned after that of Cebeci and Smith (ref. 5). The Cebeci-Smith model is difficult to use with Navier-Stokes equations because of the necessity for determining the displacement thickness. The Baldwin-Lomax model does not require the location of the outer edge of a thin-shear layer. It uses the distribution of vorticity to determine the length scale in the outer region of the shear layer. Consequently, it also uses vorticity in the inner region.

The nondimensional eddy viscosity is represented by

$$\mu_t = Re\rho\alpha\nu\ell(\gamma_k)_b \quad (12)$$

In the inner layer, $0 \leq y \leq y_c$, the expressions for v and ℓ are

$$(v)_{inner} = \ell|\omega| \quad (13)$$

$$(\ell)_{inner} = 0.4y \left[1 - \exp\left(-\frac{y^+}{26}\right) \right] \quad (14)$$

where ω is vorticity, and where

$$y^+ = y \left[\frac{Re\rho|\omega|}{\mu} \right]_w^{1/2}$$

In the outer region, $y > y_c$, the expressions for v and ℓ are

$$(v)_{outer} = \text{minimum of} \left(\mathcal{F}_{max}, \frac{(U_{max} - U_{min})^2}{4\mathcal{F}_{max}} \right) \quad (15a)$$

$$(\ell)_{outer} = y_{max} C_{BL} \quad (15b)$$

where U is the absolute value of velocity, and where the value of C_{BL} is 1.6. Instead of using equation (15a), we have used the following expression

$$(v)_{outer} = \text{minimum of} \left(\mathcal{F}_{max}, \frac{(U_{\mathcal{F}_{max}} - U_{min})^2}{\mathcal{F}_{max}} \right) \quad (15c)$$

which has been used by Baldwin since the publication of reference 2. The function $\mathcal{F}(y)$ is defined to be

$$\mathcal{F}(y) = y|\omega| \left[1 - \exp\left(-\frac{y^+}{26}\right) \right] \quad (16)$$

and the quantity \mathcal{F}_{max} is the maximum value of $\mathcal{F}(y)$ that occurs in this equation, and y_{max} is the value of y at which it occurs.

Baldwin and Lomax (ref. 2) simulated the effect of intermittency by using

$$(\gamma_k)_b = \left[1 + 5.5 \left(\frac{C_k y}{y_{max}} \right)^6 \right]^{-1} \quad (17)$$

where $C_k = 0.3$. Further, they simulated the effect of transition by setting μ_t equal to zero everywhere in a normal profile for which the maximum tentatively computed value of μ_t from the foregoing relations is less than a specified value. They have recommended the following condition

$$\mu_t = 0 \quad \text{if} \quad (\mu_t)_{max} < 14\mu_\infty$$

Visbal and Knight (ref. 19) and York (ref. 20) evaluated the Baldwin-Lomax turbulence model for two-dimensional turbulent boundary-layer computations. These investigators made

a comparison with the Cebeci model. Based on these comparisons, they recommend that the constants C_{BL} and C_k should be, respectively, equal to 1.2 and 0.646 for $M_\infty = 0.01$. This value of C_{BL} would give a lower value of skin friction than that with the value of 1.6 used in this study.

The Baldwin-Lomax turbulence model is deficient in three aspects, and it gives erroneous results for one situation. First, it does not simulate the transition process. There is an abrupt change in μ_t from a value of zero in laminar flow to a nonzero value in turbulent flow. This is corrected by including the transition factor given in equation (8). Second, the model is not valid in the far-wake region since the inner eddy-viscosity formulation extends to large values of y ; therefore, it dominates the outer or wake eddy-viscosity formulation. In the present study, this anomaly has not been corrected, since the grid system is not appropriate in the TLNS computations. And third, the model does not account for the effect of pressure gradient. This deficiency is also not eliminated. The model erroneously gives $\mu_t = 0.0$ in the wake region when the wake is symmetric, because the Van Driest damping function, equation (14), depends on the vorticity on the centerline of the wake, which has the value of zero. This error has been corrected by the expression

$$(\mu_t)_b = Re \rho \alpha \nu \ell \gamma_{tr} (\gamma_k)_b \quad (18)$$

with the length scale equation now given by

$$(\ell)_{inner} = 0.4y \left[1 - \exp \left(-\frac{y^+}{26} - \frac{\chi^+}{26} \right) \right] \quad (19)$$

with

$$\chi = \begin{cases} 0.0, & \text{if } x \leq 1.0 \\ (x - x_{te}), & \text{otherwise} \end{cases}$$

In the outer region, the expressions for v and ℓ are the same as those given in equations (15b) and (15c), but the definition of $\mathcal{F}(y)$ is replaced by the following:

$$\mathcal{F}(y) = y|\omega| \left[1 - \exp \left(-\frac{y^+}{26} - \frac{\chi^+}{26} \right) \right] \quad (20)$$

Transition Criteria

There are a few empirical methods for computing the location at which a laminar flow begins to undergo transition to a turbulent flow. The transition location is fixed by experimental observation, by laminar separation, or by Michel's correlation method (ref. 21). Michel's method is not valid for flows with separation; instead it is assumed that the computed laminar separation location is the transition location. Michel's method is embodied in the equation of reference 22, that is,

$$Re_{\theta_{tr}} = 1.174 \left(1 + \frac{22,400}{Re_{x_{tr}}} \right) Re_{x_{tr}}^{0.46} \quad (21)$$

where subscripts θ and x designate Reynolds numbers based on momentum thickness and surface distance, respectively.

Various Models

The turbulence models and transition criteria have been used in the combinations of table 1. For example, Model III is a combination of the wake formulation of model $(\mu_t)_a$ and of the boundary-layer formulation of model $(\mu_t)_b$ with the empirical transition criteria. Models I-IV are used in the IBL method, whereas only Models II and V are used in the TLNS method. It was not feasible to use model $(\mu_t)_a$ and Model III with the latter method because of large fluctuations in the location of the edge of the boundary layer during the iterative solution procedure.

TABLE 1. - COMBINATION OF TURBULENCE MODELS AND TRANSITION CRITERIA.

MODEL	x_{tr}		$(\mu_t)_a$		$(\mu_t)_b$	
	EMP.	EXP.	B. L.	WAKE	B. L.	WAKE
I	✓		✓	✓		
II	✓				✓	✓
III	✓			✓	✓	
IV		✓	✓	✓		
V		✓			✓	✓

Note: EMP. = empirical; EXP. = experimental; B. L. = boundary layer.

DISCUSSION OF RESULTS

We have chosen a flow over a NACA 0012 airfoil section for which to compare the TLNS and IBL computations with measurements, and with each other. Two entirely different experiments at almost the same Reynolds number are chosen in order to compare not only the computations with data, but also to compare data of one experiment against the other. The experimental data, reported by Gregory and O'Reilly (ref. 23), were obtained during their Session III at $Re = 2.88 \times 10^6$ and $M_\infty = 0.16$ on a clean (smooth) airfoil, and those reported by Loftin and Smith (ref. 24) were determined at $Re = 3 \times 10^6$ and $M_\infty = 0.07$.

The IBL computations are done at $M_\infty = 0.0$ assuming that the fluid is incompressible, whereas the TLNS computations are carried out at $M_\infty = 0.1$. The latter computations could have been done at the experimental Mach numbers, but this was not done; the reason it was not done was the desire to have the same Mach-number influence in both sets of TLNS computations for comparison with the IBL computations, and to keep the Mach number low enough for the TLNS computations without requiring excessive computational times. Anyway, the computational Mach numbers are low enough for compressibility to have little influence, even at maximum lift. This can be verified from the computed Mach-number contours shown in figure 1. Most of the compressibility effect is near the nose of the airfoil, where the maximum local Mach number is 0.35.

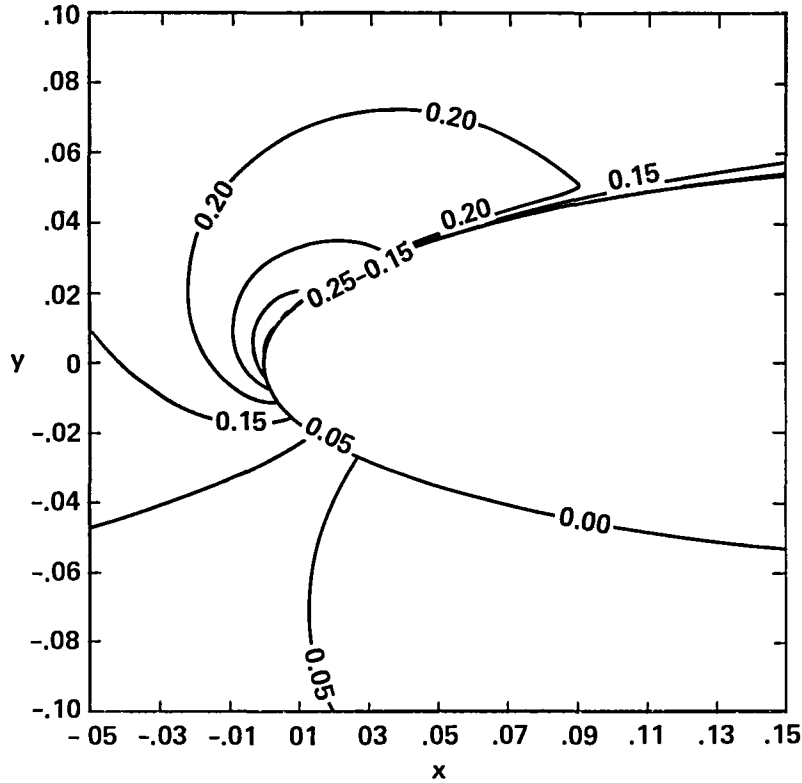


Figure 1. - Mach-number contours: NACA 0012, $Re = 2.88 \times 10^6$, $\alpha = 16^\circ$, and $M_\infty = 0.1$.

Computational Grids

The total number of grid points used in the TLNS calculations is based on the decision to use about 85% of in-core memory of one processor of the CRAY X-MP 22 computer. These calculations made use of a C-type-grid topology with 257×57 node points, and with 36 points in the wake region of the airfoil along the free-stream direction. It was generated with an algebraic grid generator called CGUAVA based on a procedure formulated by Eiseman (ref. 25). Except near the leading edge and the trailing edge of the airfoil, the first grid point off the airfoil surface is at a distance of $0.00001L$, where L is the chord length. For fully developed, attached turbulent boundary layers, this distance corresponds to y^+ at the first grid point off the surface in the range of 0.15 to 3.5, depending on chordwise location and angle of attack, at $Re = 2.88 \times 10^6$. The first grid point upstream of the leading edge and downstream of the trailing edge is at a distance of $0.001L$. The outer boundary is kept at 10 chord lengths from the airfoil. Figure 2 shows a part of the grid system.

The IBL calculations were performed with approximately 80 x-stations on the upper surface and approximately 60 on the lower surface, and with 37 y-stations for small angles of attack and 50-70 for large angles of attack; the y-stations were on the upper surface from the leading-edge region to the trailing edge of the airfoil. There are 30 x-stations in the wake, which extends up to 3 chord lengths downstream of the trailing edge.

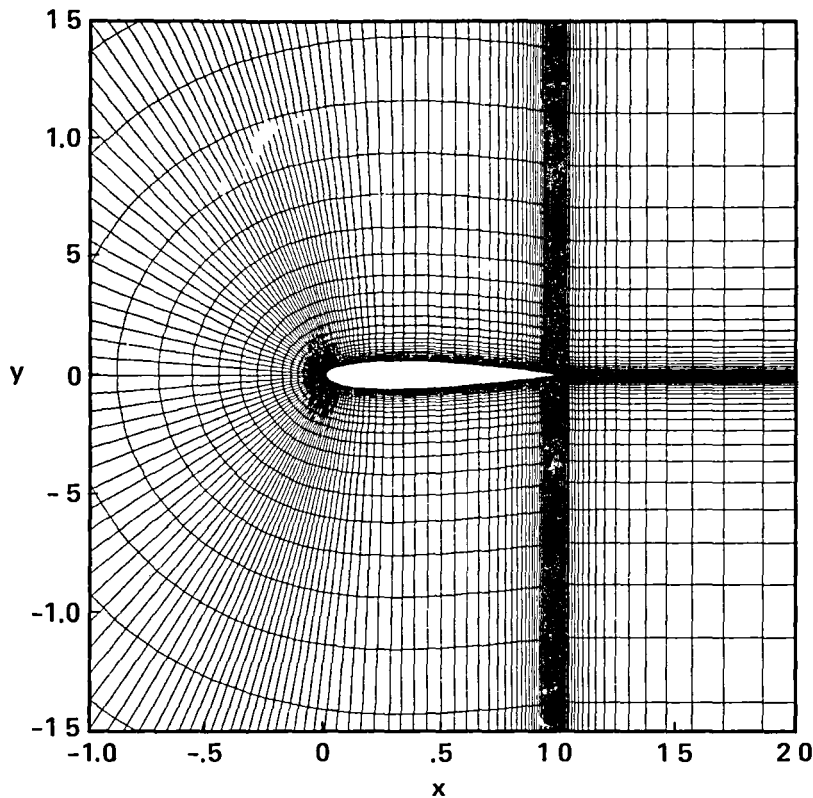


Figure 2. - C-grid around the NACA 0012 airfoil.

Transition Locations

Figure 3 shows the transition locations: computational, experimental, and empirical locations based on Michel's correlation method. Here lower surface transition locations at positive incidence are plotted as if they were upper-surface locations at negative incidence. The transition locations are fixed for $Re = 2.88 \times 10^6$ as follows: When no transition bubble is experimentally observed, both IBL and TLNS computations have used the experimental transition locations. When this bubble is observed, the IBL computations have considered transition location at the experimental laminar separation point, whereas the TLNS procedure has taken this location to be approximately at the streamwise center of the bubble. The actual computational transition locations are slightly different from these locations owing to the fact that there may not be a grid point at the experimental locations. In addition to these computations, computations have been made with the IBL method using the empirical locations. On the other hand, at a Reynolds number of 3.0×10^6 , both procedures have used empirically computed transition locations. Again, the TLNS computational locations are slightly different owing to the fact that there may not be a computational grid point exactly at the empirical location.

As can be seen from figure 3, for $Re = 2.88 \times 10^6$ the differences in the locations of transition arrived at by experiment and the previous procedures were largest, approaching 10% of chord, at low angles of attack. On the upper surface, at these angles, the influence of transition is small. The discrepancies associated with angles of attack greater than 9° stem from the different approaches

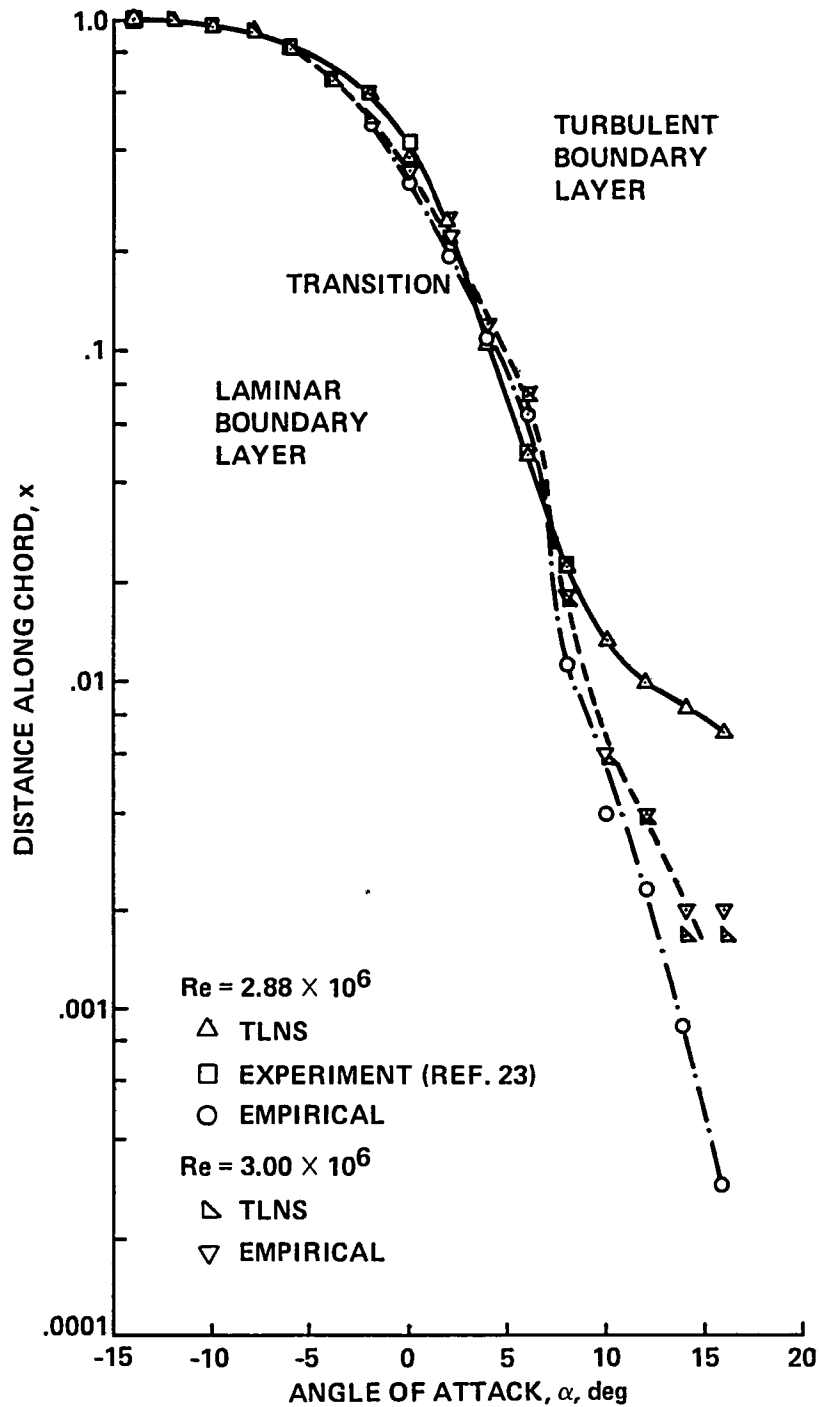


Figure 3. - Transition locations on the NACA 0012 airfoil.

to the transition location in the presence of a separation bubble; the largest discrepancy is less than 1% of chord, which is within measurement precision. Furthermore, on the upper surface of the airfoil, empirical locations are upstream of the experimental transition locations or laminar separation points, except at angles of attack of 4° and 6° . For $Re = 3 \times 10^6$, the empirical

locations on the upper surface of the airfoil are downstream of those for $Re = 2.88 \times 10^6$. This should not be the case, and at present we have no explanation for it.

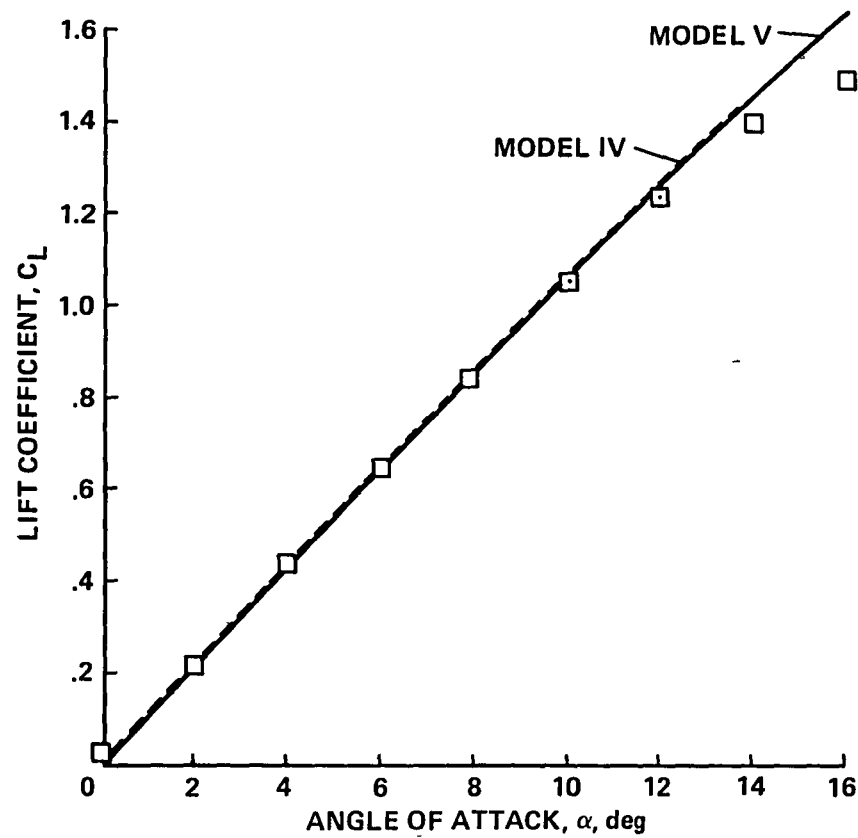
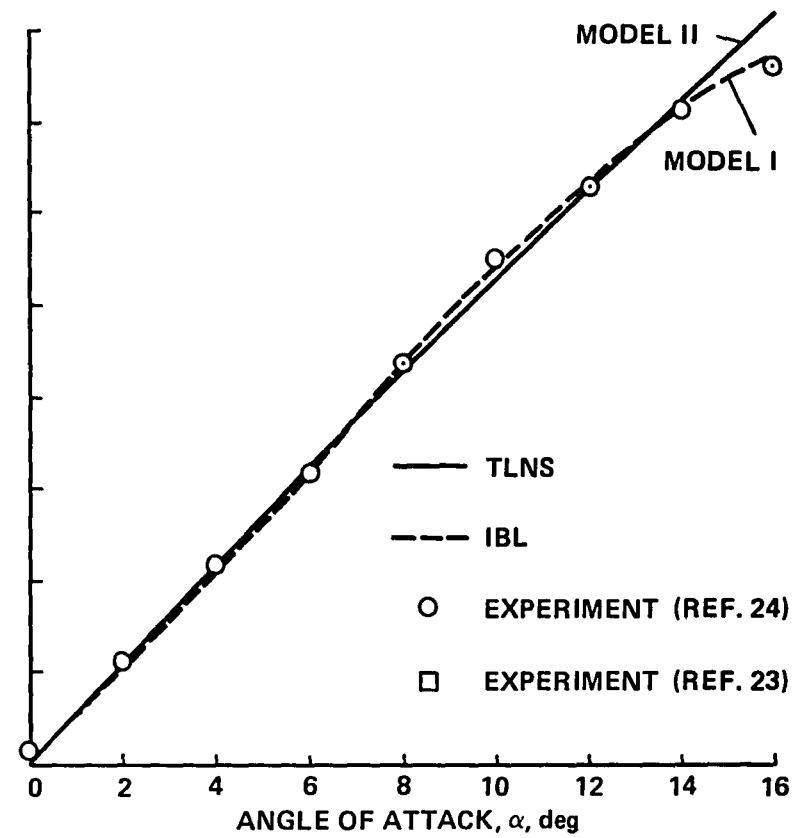
Comparisons of Loads

The calculated and measured values of lift coefficient C_L are shown in figure 4 as a function of angle of attack, and they are in close agreement up to 12° . At $\alpha = 16^\circ$, the IBL approach did not work with Model IV, but it did work with Model I (tables 1-3, and fig. 4). The only difference between these two models is the specification of the transition location, being, for example, at 0.8% of chord for Model IV and at 0.03% for Model I at $Re = 2.88 \times 10^6$. At higher angles of attack, the expected fall off in C_L does not occur. However, as it is shown in reference 1, a small change in the location of transition can cause lower values of calculated C_L . The magnitude of the required change in the location of transition is similar to that which can be resolved experimentally. The TLNS approach cannot predict this effect, probably because of the following reasons: (1) it does not use a time-accurate numerical scheme, a requirement for predicting stalling characteristic, which is by definition unsteady; and (2) the normal pressure gradient at the surface of the airfoil is assumed to be negligible. On the other hand, the IBL approach does a better job of predicting this lift fall off than the TLNS approach. This conclusion is misleading because, if the wake curvature effect were included in the IBL approach then the lift coefficient would be slightly higher than that computed.

TABLE 2. - LIFT AND DRAG COEFFICIENTS
FOR THE NACA 0012 AIRFOIL AT $Re = 2.88 \times 10^6$.

α , deg	C_L				C_D			
	EXP.	IBL		TLNS	EXP.	IBL		TLNS
		I	IV	V		I	IV	V
0	0.025	0.0	0.0	0.0	0.0069	0.00596	0.00562	0.00568
2	0.220	0.209	0.205	0.213	0.0073	0.00611	0.00571	0.00572
4	0.440	0.421	0.418	0.430	0.0080	0.00633	0.00689	0.00750
6	0.650	0.639	0.637	0.641	0.0094	0.00689	0.00781	0.00921
8	0.850	0.873	0.856	0.857	0.0112	0.00899	0.00921	0.01207
10	1.055	1.077	1.081	1.065	0.0134	0.01070	0.01136	0.01547
12	1.240	1.256	1.268	1.265	0.0180	0.01294	0.01306	0.01962
14	1.400	1.422	1.448	1.457	0.0244	0.01662	0.01447	0.02469
16	1.490	1.545		1.640	0.0338	0.02315		0.03121

The influence of the turbulence model was also investigated, and the results are presented in tables 2 and 3. The effect on C_L for $Re = 2.88 \times 10^6$ is negligible, except at $\alpha = 16^\circ$, as discussed

(a) $Re = 2.88 \times 10^6$ (b) $Re = 3.0 \times 10^6$ Figure 4. - Variation of C_L with α for the NACA 0012 airfoil.

above. The lift coefficients for $Re = 3.0 \times 10^6$ are nearly the same up to $\alpha = 10^\circ$ for turbulence Models I, II, and III. When the angles of attack are greater than 10° , the IBL approach does not converge with Model II, and lift values obtained with Model III are not satisfactory. The TLNS approach does not converge with Models I and III primarily owing to the numerical scheme that is not time-accurate.

TABLE 3. - LIFT COEFFICIENTS FOR THE NACA 0012 AIRFOIL AT $Re = 3.0 \times 10^6$.

α , deg	C_L				
	EXP.	INTERACTIVE			TLNS
		I	II	III	II
0	0.03	0.0	0.0	0.0	0.0
2	0.23	0.2097	0.2130	0.2131	0.2166
4	0.44	0.4202	0.4265	0.4266	0.4310
6	0.64	0.6372	0.6472	0.6488	0.6450
8	0.88	0.8726	0.8832	0.8818	0.8599
10	1.10	1.0775	1.1110	1.1102	1.0614
12	1.26	1.2665		1.3143	1.2608
14	1.43	1.4293		1.5190	1.4489
16	1.52	1.5449		1.7163	1.6313

As shown in figure 5, a comparison of the NACA data (ref. 24), the NPL data (ref. 23), and the NASA data (ref. 26) in terms of the lift-curve slope using Kaplan's rule (ref. 27), raises some question concerning the NACA data. Both the IBL and TLNS procedures give lift-curve slopes that compare well with the NPL and NASA data.

The drag results of tables 2 and 4, and figure 6 require more detailed discussion. The IBL approach has used the velocity defect in the wake to compute the drag coefficient C_D , whereas, the TLNS procedure has integrated forces around the airfoil surface. The pressure drag ranges from about 13% to 86% of the total drag, for angles of attack of 0° to 16° . It is likely that the pressure drag integrated using surface-pressure distribution is determined with acceptable accuracy, especially in view of the quality of the calculations suggested by the comparisons of computed and experimental pressure coefficients discussed below. At zero angle of attack, the total drag computed by the IBL method is within two counts in hundred thousandths and in ten thousandths, respectively, for $Re = 2.88 \times 10^6$ and $Re = 3.0 \times 10^6$, of that computed by the TLNS method; and both values agree well with the experimental values. At angles of attack of 0° and 2° , the total drag computed by the IBL method is within six counts (hundred thousandths) of that computed by the TLNS method, with both methods utilizing experimental transition locations; values of both methods agree well with the experimental values. At higher angles of attack, before the appearance of the transitional bubble, the computed results of the IBL method are lower than those determined by experiments and the TLNS method. At still higher angles of attack in the presence of this bubble, with turbulent flow separation and lower pressure coefficients along the aft region of the upper surface, the IBL values are still lower. This drop is probably a result of the fact that the wake-curvature effect and the cross-stream pressure gradient effect are not accounted

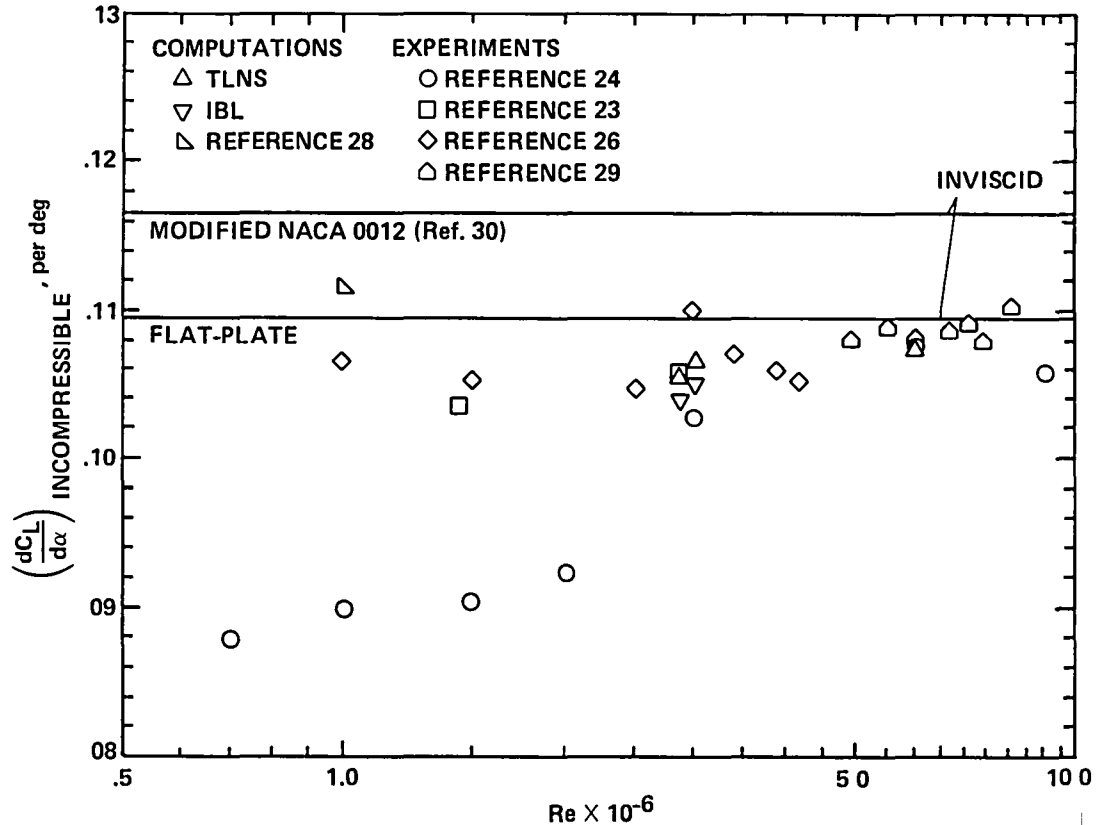


Figure 5. - Lift-curve slope for the NACA 0012 airfoil.

for in this approach. The cross-stream pressure gradient increases the momentum thickness of the wake, and consequently, the total drag. This conjecture is consistent with the findings of reference 6, in which the use of the present $(\mu_t)_a$ formulation for wake flows was examined.

The influence of the turbulence model as indicated in tables 2 and 4, although more pronounced in C_D than in C_L , is unlikely to explain the discrepancies of figure 6. If the values of constants C_{BL} and C_k recommended in references 19 and 20 were used in the formulation of $(\mu_t)_a$, then the friction drag coefficients would be lower than those computed with the present formulation.

Further examination of the experimental values of C_D showed that they are different from those reported by Loftin and Smith (ref. 24) for $Re = 3.0 \times 10^6$. For example, at an angle of attack of 12° the latter NPL reference has reported C_D higher by 14%. Since the NPL data are dated 25 years later than those of reference 24, they are probably more accurate. The TLNS procedure appears to do a better job of predicting drag than the IBL procedure, which underpredicts at high angles of attack. However, it is evident that the uncertainties associated with the calculation procedures and with measurement of C_D require further examination.

The experimental moment-characteristic documented in the NACA report is quite different from that documented in the NPL report (fig. 7). Assuming that the latter data are accurate, the TLNS procedure does not well predict the moment coefficient at high angles of attack.

A study was conducted to provide some indication of the influence of the outer boundary conditions on loads acting on the airfoil using the TLNS approach. Two different locations are

TABLE 4. - DRAG COEFFICIENTS FOR THE NACA 0012 AIRFOIL AT $Re = 3.0 \times 10^6$.

α , deg	C_D				
	EXP.	INTERACTIVE			TLNS
		I	II	III	II
0	0.0059	0.00585	0.00592	0.00595	0.00614
2	0.0062	0.00606	0.00608	0.00619	0.00632
4	0.0070	0.00635	0.00645	0.00648	0.00734
6	0.0084	0.00700	0.00704	0.00700	0.00885
8	0.0100	0.00881	0.00892	0.00899	0.01227
10	0.0130	0.01062	0.01065	0.01071	0.01585
12	0.0158	0.01260		0.01261	0.02005
14	(0.0204)	0.01638		0.01495	0.02567
16	(0.0264)	0.02315		0.01853	0.03206

Note: The values in parenthesis are determined by extrapolation.

considered for the outer boundary: 10 chord lengths and 20 chord lengths from the trailing edge. The increase in the distance from 10 to 20 chord lengths is achieved by adding grid points, resulting in a 273×65 grid-system with 44 grid points in the wake, such that the grid distribution in the vicinity of the airfoil is essentially identical for these two different locations of the outer boundary. Further, computations are carried out with and without the circulation correction (ref. 11) to the free-stream values, as discussed in the appendix. The results of this study are shown in figure 8 for $\alpha = 2^\circ$. The variations in the lift, drag, and moment coefficient are, respectively, 1%, 6 counts (hundred thousandths) or 1%, and 4.5%. These variations for lift and drag coefficients are within the experimental accuracy. Therefore, all results presented in this report, except those mentioned in figure 8, have been obtained with a 257×57 grid-system, with the outer boundary at 10 chord lengths, and without the circulation correction

Some Flow-Field Details

Distributions of pressure coefficient are shown on figures 9-12. Figures 9 and 10 compare the TLNS and IBL results, respectively, with the experimental data of reference 23 for a range of angles of attack; and figure 11 compares the results of the two procedures for angles of attack of 10° and 12° . As can be seen, the calculated results of the two procedures agree very well with each other and also with the experimental data. In figure 9, at 14° and 16° , the TLNS results show some irregularities near the suction peak. This is caused by improper transition location. This conclusion is supported by the results shown in figure 12. There is no irregularity at the above angles of attack, but there is at the angle of attack of 6° . The latter is caused by the computational transition location being downstream of the possible experimental location. Such an irregularity is not there at the corresponding angle of attack at $Re = 2.88 \times 10^6$ (fig. 9). Observe that the empirical transition location at $Re = 3 \times 10^6$ is downstream of that at

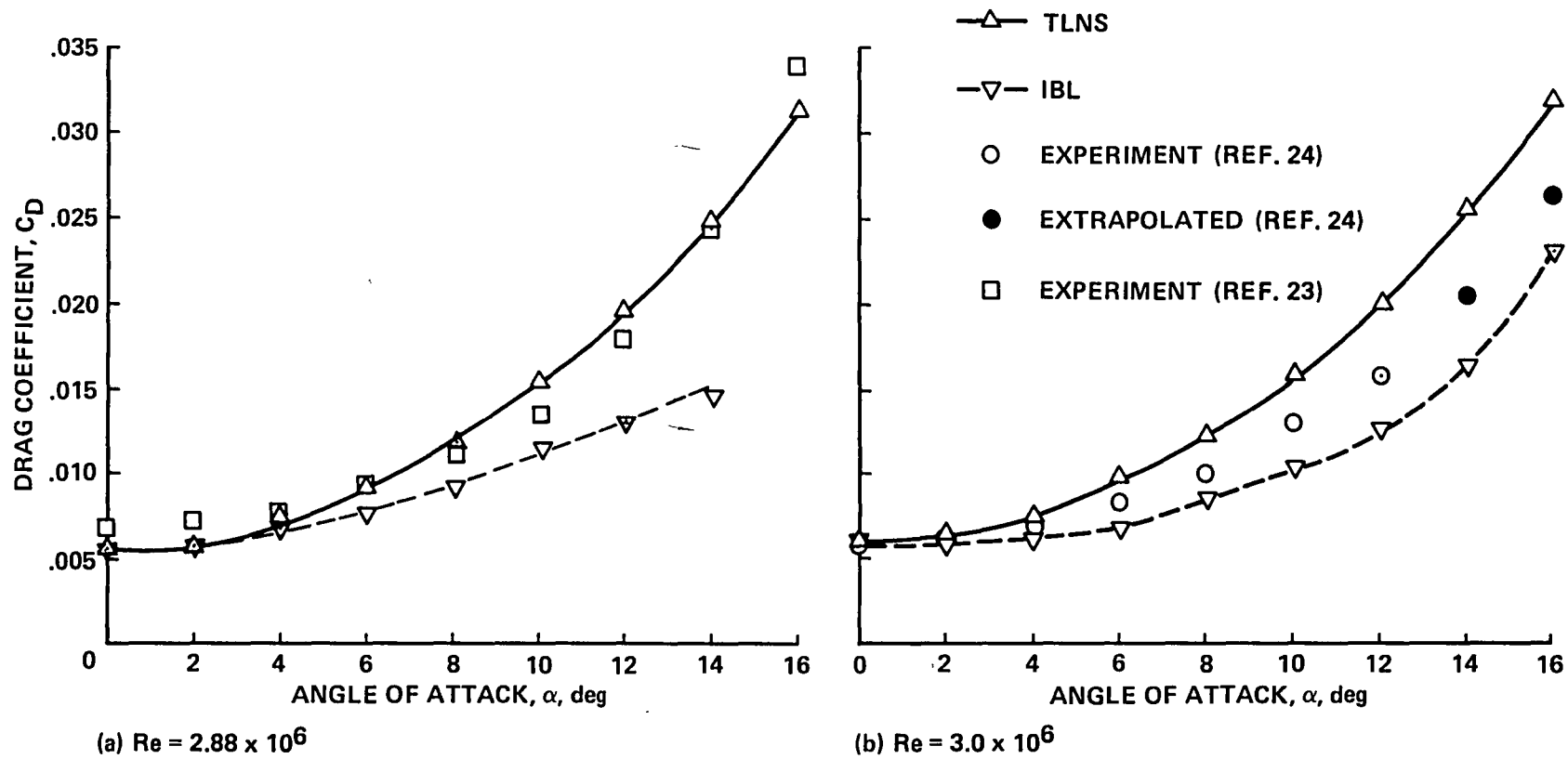


Figure 6.- Drag characteristic of the NACA 0012 airfoil.

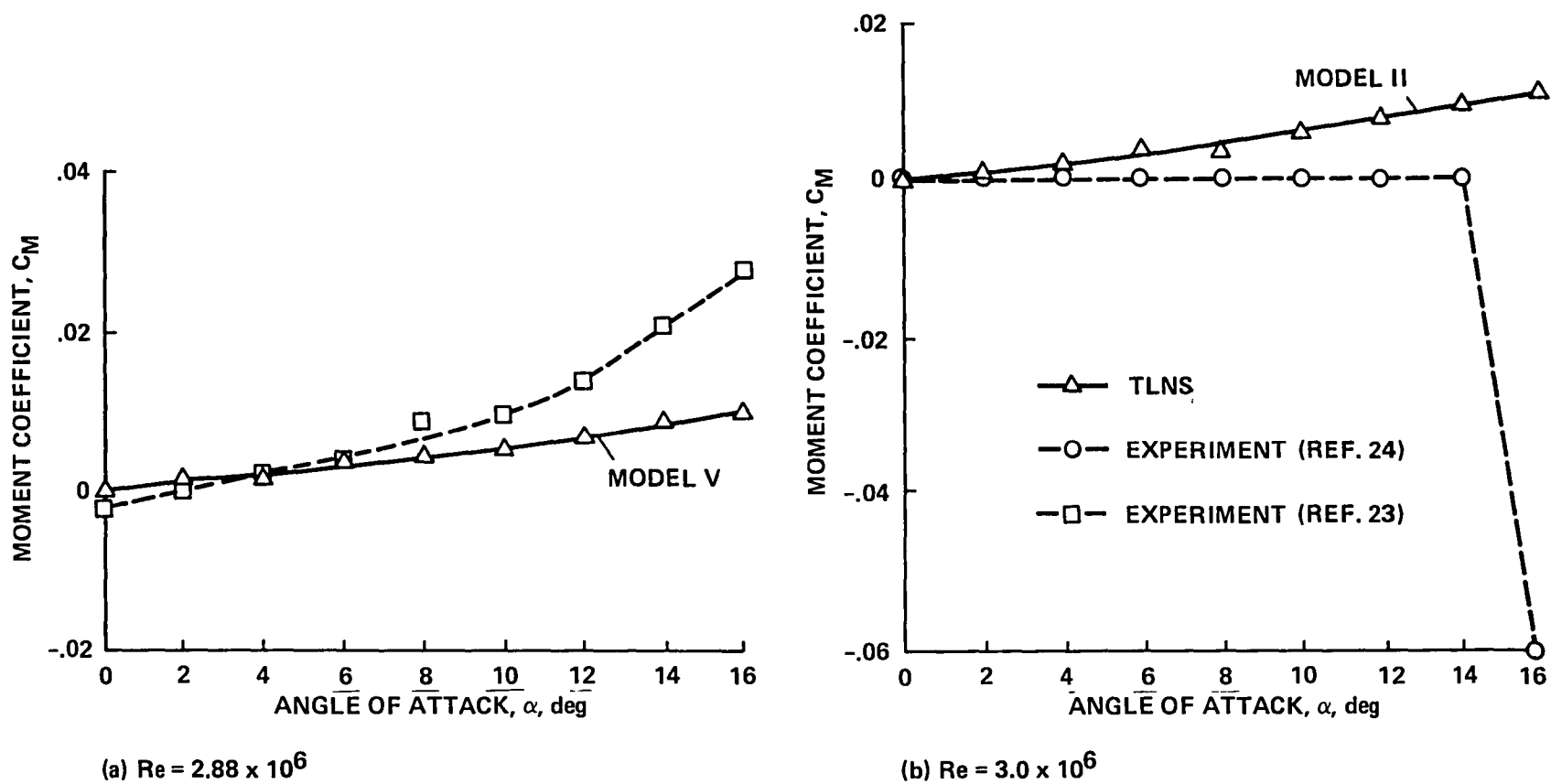


Figure 7. - Moment coefficients for the NACA 0012 airfoil.

$Re = 2.88 \times 10^6$, both being downstream of the experimental location at the lower Reynolds number.

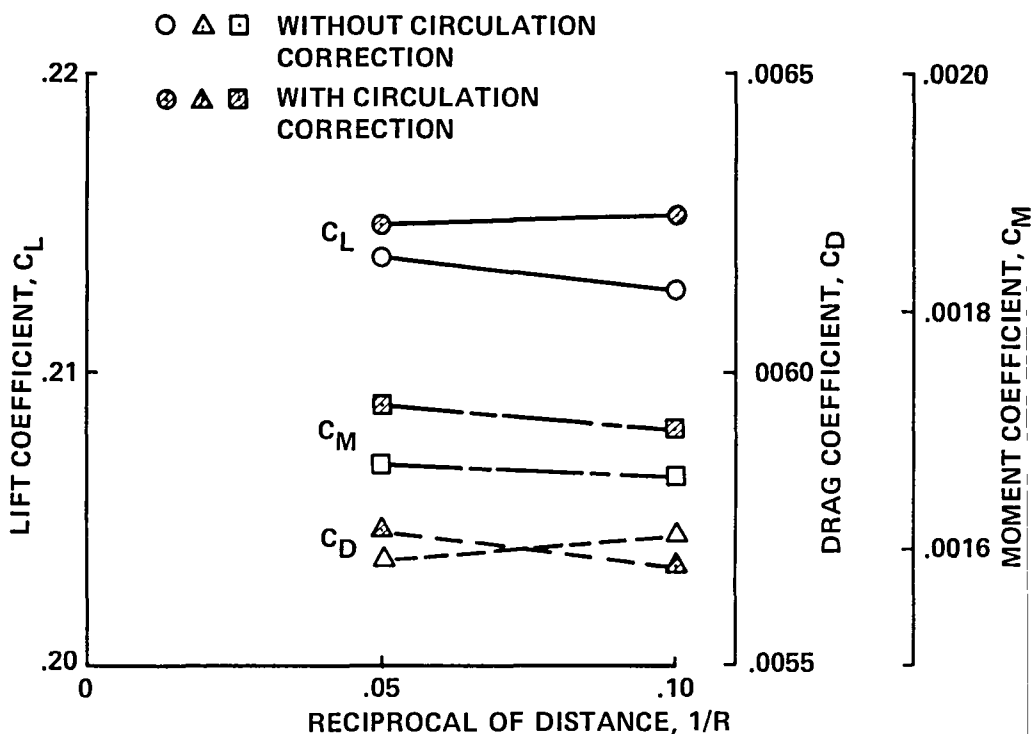


Figure 8. - Effect of outer boundary conditions on loads:
NACA 0012, $Re = 2.88 \times 10^6$, $M_\infty = 0.2$, $\alpha = 2^\circ$.
0.1

Pressure contours around the leading edge and the trailing edge of the airfoil at $\alpha = 2^\circ$ and 14° are shown in figure 13. The normal pressure gradient near the leading edge is negligible at small angles of attack, but not at large angles of attack. For the range of angles of attack investigated, immediately downstream of the trailing edge the normal pressure gradient is negligible. These conclusions are confirmed by the streamline plots. As shown in figure 14, the streamline curvature effects are expected to be important at high incidences near the leading edge, and in the wake region where the flow tends to go back to the free-stream direction.

Calculated distributions of displacement thickness δ^* are reproduced in figure 15. Corresponding experimental data are not available, but the results are interesting in that they show the rapid growth of δ^* with angle of attack; and both numerical schemes give similar results. Because of the uncertainty of defining the edge of the boundary layer with the grid system used near the aft portion of the airfoil in the TLNS method, the smaller of (1) the inviscid velocity at the surface of the airfoil, based on the Bernoulli's equation and the ideal gas relation, and (2) the maximum velocity along the grid line emanating from the surface, is taken as the edge velocity for computing δ^* . Consequently, there is a kink in the δ^* distribution when a switch is made from one family of edge velocities to the other.

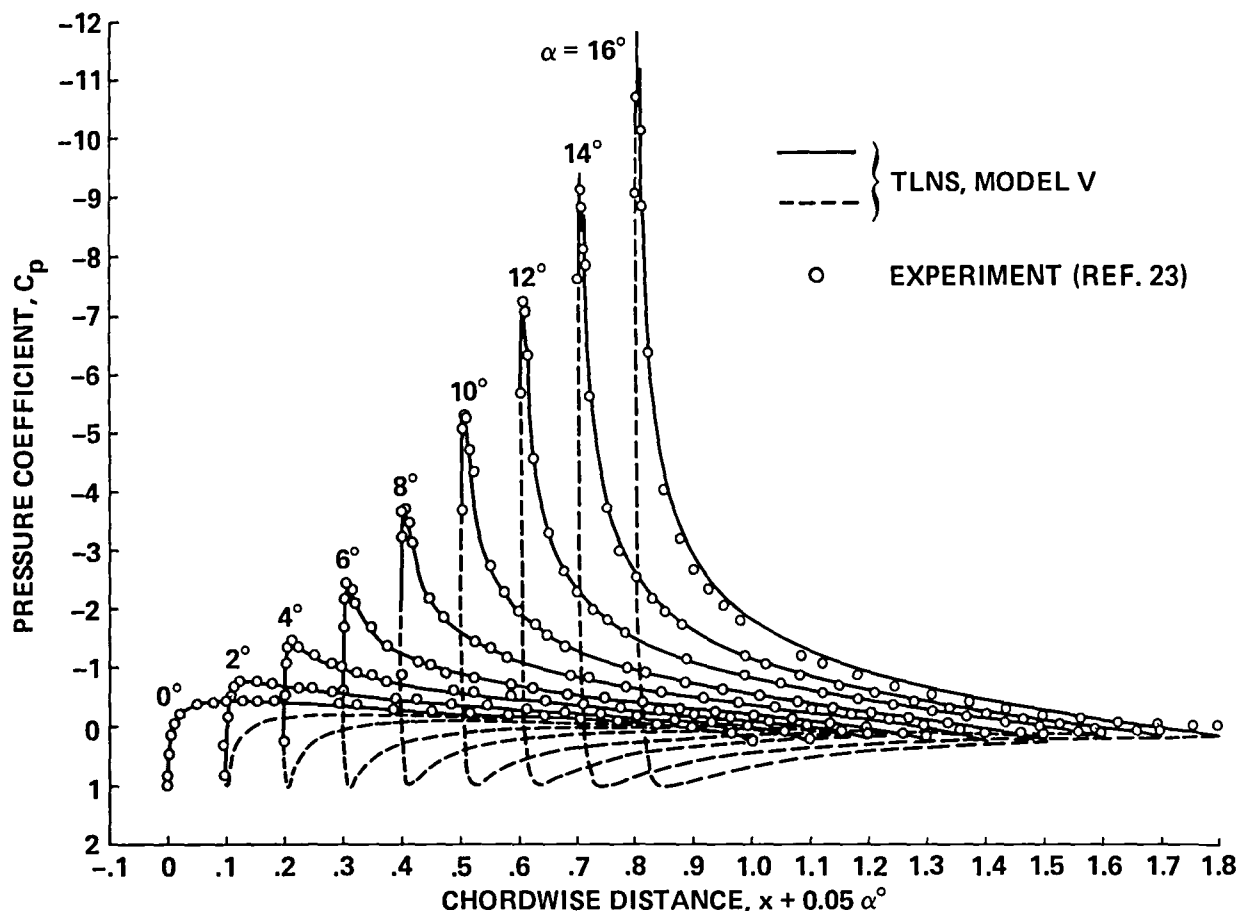


Figure 9. - Comparison of pressure distributions: TLNS results and experimental data at $Re = 2.88 \times 10^6$.

The TLNS method is able to compute transitional separation bubbles. With a Navier-Stokes procedure, this is the first time such a bubble has been predicted as a part of the overall problem of computing the flow past an airfoil. Figure 16 shows that the computed separation and reattachment points do not agree with the experimental points. In addition to this, the computation shows a transitional bubble at $\alpha = 8^\circ$, whereas the experiment does not. These differences are owing to the lack of grid resolution, to imprecise computational transition location, and to experimental inaccuracies associated with a small transition bubble.

The influence of transition location on a transitional separation bubble is illustrated in figure 17. If the transition location is upstream of the location where it should be, the transition bubble cannot be observed in computation (curve (a) of fig. 17). On the other hand, if it is downstream of the location where it should be, it is difficult to get a converged solution, supporting a conclusion by Cebeci et al. (ref. 1) and by Carr and Cebeci (ref. 31) from calculations based on the IBL method. Cases (c) and (d) in figure 17 are solutions at two different iteration numbers with the transition location being the same. It was not possible to obtain a converged solution. Cases (a) and (b) are converged solutions.

Turbulent separation regions from the TLNS method are reported in figure 18. Note that

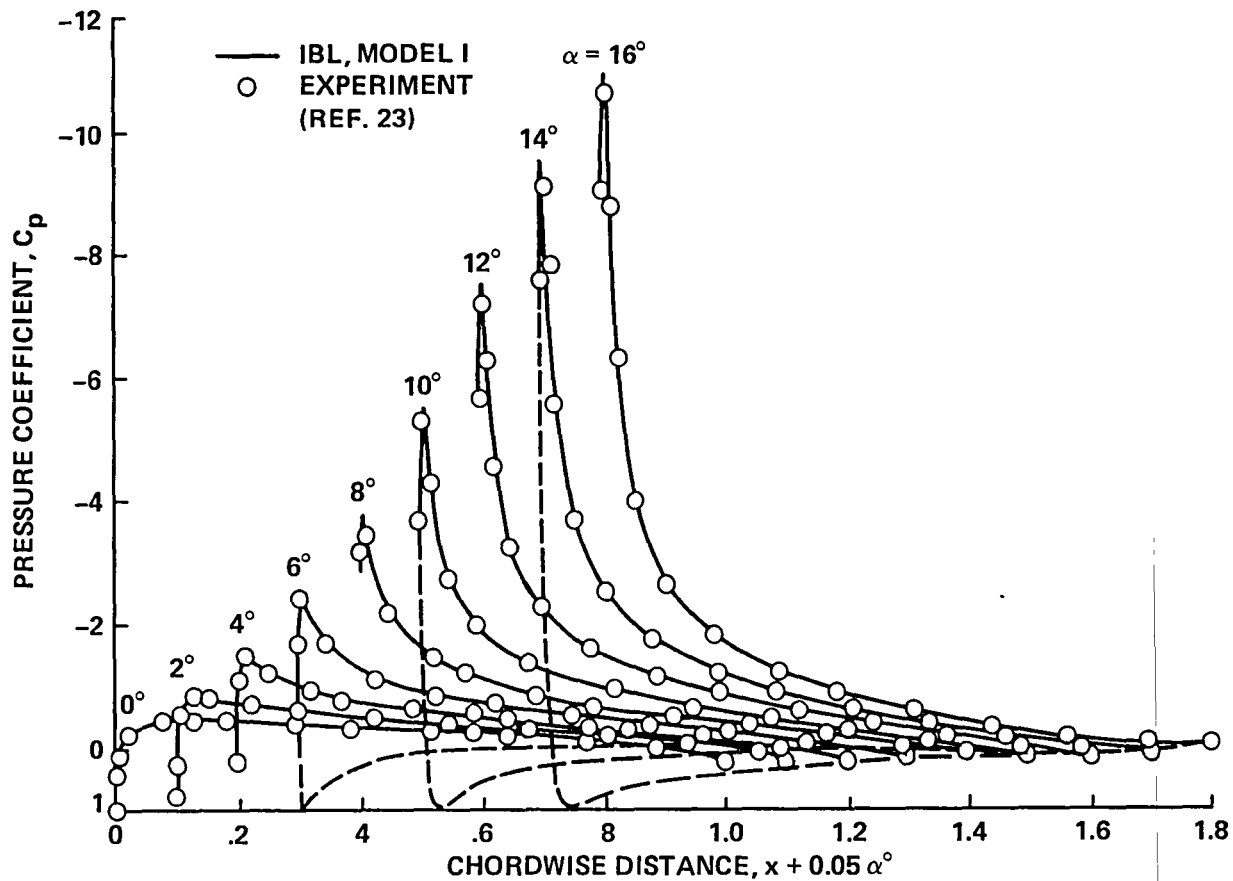


Figure 10. - Comparison of pressure distributions: IBL results and experimental data at $Re = 2.88 \times 10^6$.

in this figure the vertical scale is 20 times larger than the horizontal scale. Experimental and computed separation points from TLNS and IBL computations do not agree, probably owing to a lack of grid resolution, turbulence model, and experimental inaccuracies.

Computational Efficiency

The evaluation of the two procedures can be made, in part, by information of the type referred to in the previous paragraphs. It is often necessary also to consider the cost and ease of achieving the results. In this respect, it is important to note that one iteration of the IBL procedure and that of the TLNS procedure require about 0.1 min of CPU time on an IBM 3381 computer and about 0.005 min on one processor of a CRAY X-MP 22 computer, respectively. The latter procedure, *which is not developed for computing flows of essentially incompressible fluid*, is quite costly. For the IBL method, the convergence criterion is 0.1% residual in the conservation of momentum, requiring up to approximately 10 iterations; whereas, for the TLNS methods, the convergence criterion is 10^{-11} or lower residuals in the governing equations, requiring several thousand iterations.

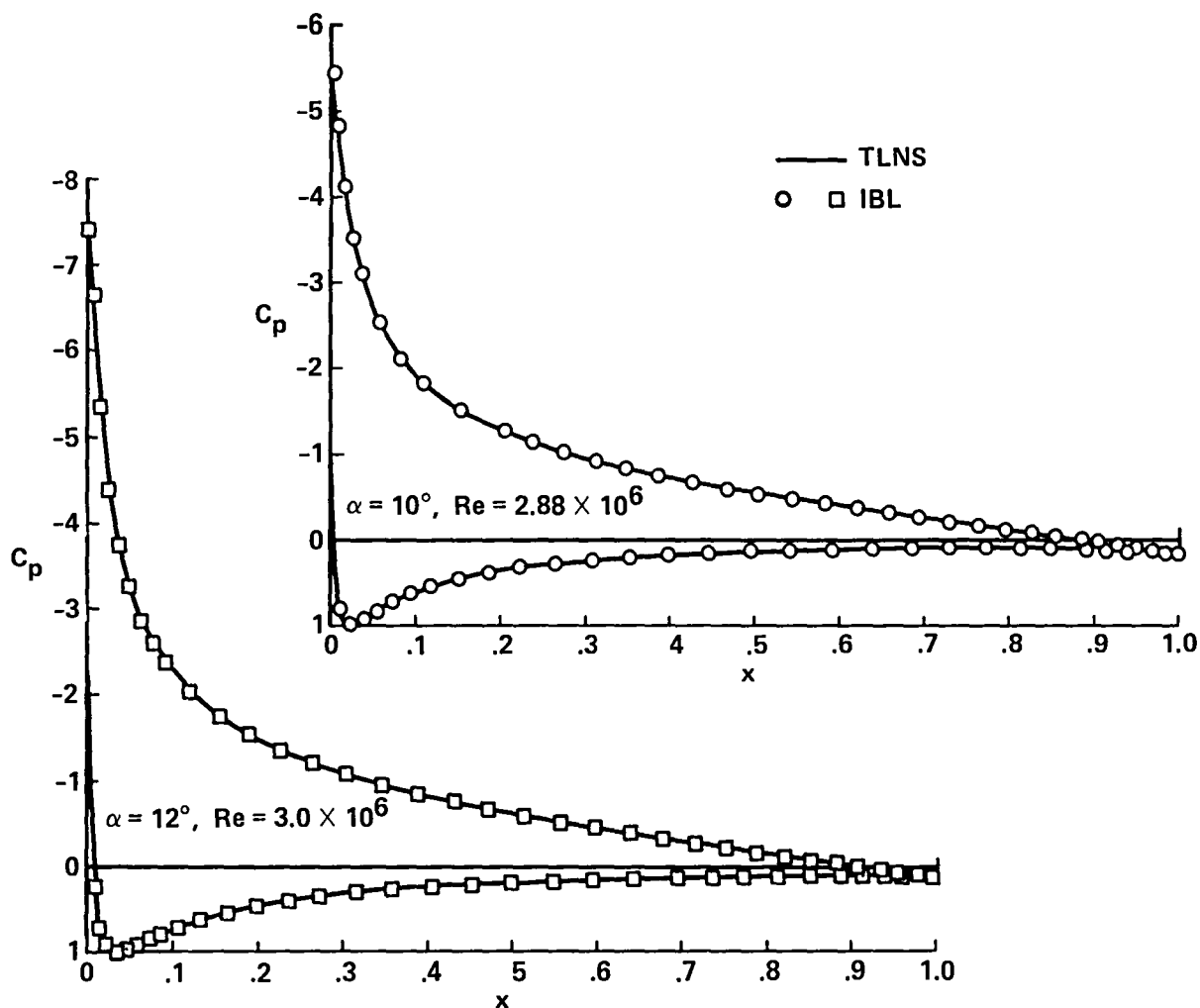


Figure 11. - Comparison of pressure distributions: TLNS and IBL results.

Different criteria are available for terminating an iterative procedure. They are based on either computational cost or computational accuracy. The primary consideration in the TLNS computations has been accuracy. Criteria based on accuracy vary from plotting or engineering accuracy to computational machine accuracy, with the former being subjective and the latter being machine dependable. This is illustrated with the convergence histories for the TLNS computation shown in figures 19 and 20.

The convergence histories of C_L and C_D shown in figure 19(a) suggests that the converged solution is achieved within 1,200 iterations. But, the machine accuracy is not achieved even after 31,000 iterations (fig. 19(d)). One percent error in C_L is achieved long before a corresponding error in C_D . An error of less than one count (ten thousandths) in C_D is reached in 14,000 iterations. On the other hand, the convergence history of the L_2 -norm of the residual of the governing equations, taken together or individually, would lead to somewhat different conclusions. An example is presented in figure 20 for the mass conservation equation. When this equation is satisfied its residual is zero. If the convergence criterion is that the residual should decrease by four orders of magnitude, then in about 1,200 iterations a converged solution is obtained, whereas

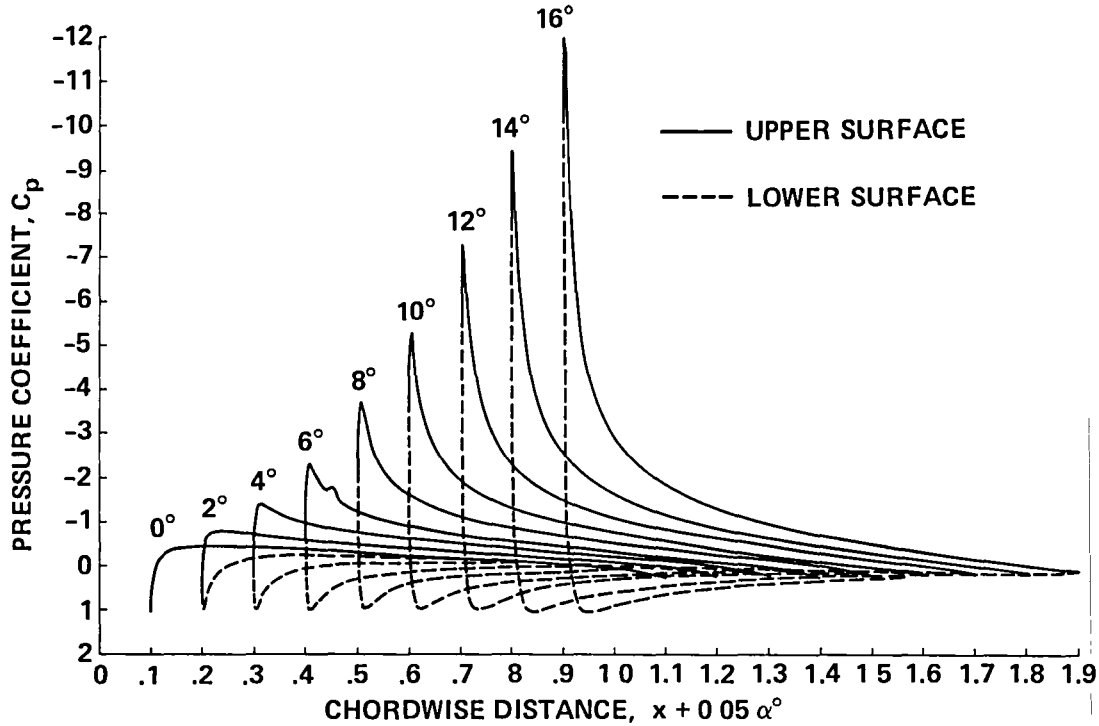


Figure 12. - Pressure distributions determined with the TLNS method and Model II
at $Re = 3.0 \times 10^6$.

the convergence criterion of six orders of magnitude results after about 6,500 iterations (fig. 20(a)). A further 15,000 iterations hardly not reduce this residual, with the residual fluctuating around 10^{-10} for the first 7,500 iterations (fig. 20(b)) and around 2×10^{-11} for the second 7,500 iterations (fig. 20(c)). Eventually, the residual does decrease monotonically as seen in figure 20(d). Again, more than 31,000 iterations are required for machine accuracy. In these computations, the reference time-step (eq. 45) was varied from 1 to 10, as it was not possible to maintain the same value for avoiding divergence.

The large number of iterations required for the TLNS is a result of the following: (1) the numerical scheme is not linearized with respect to the effective viscosity, and (2) the numerical scheme is not efficient for low Mach numbers. The latter is substantiated by the convergence histories shown in figures 21 and 22 for $M_\infty = 0.5$. A possible modification of the present scheme for efficient computations for low Mach number is discussed by Turkel (ref. 32).

UPSTREAM INFLUENCES

The boundary-layer theory is based on the assumption that the shear layer is thin and on the condition that this layer grows only slowly in the general direction of flow. As a consequence of the above assumption and condition, the upstream influence *within* the thin layer is not accounted for by the first-order theory and is only partially accounted for by the second-order theory. This is the fundamental limitation of the boundary-layer theory.

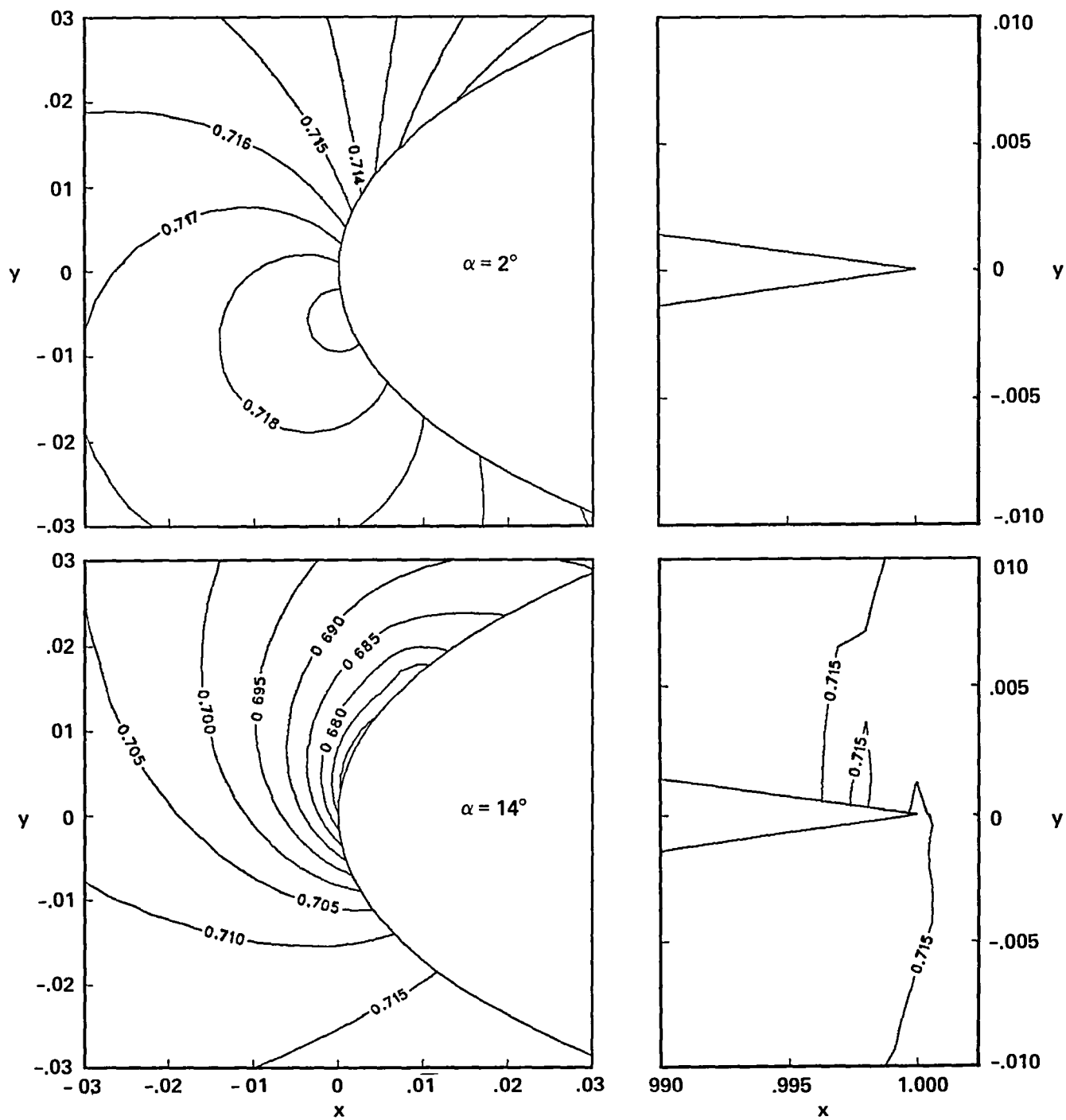


Figure 13. - Pressure contours around the nose and the tail of the NACA 0012 airfoil:
 $Re = 2.88 \times 10^6$ and $M_\infty = 0.1$.

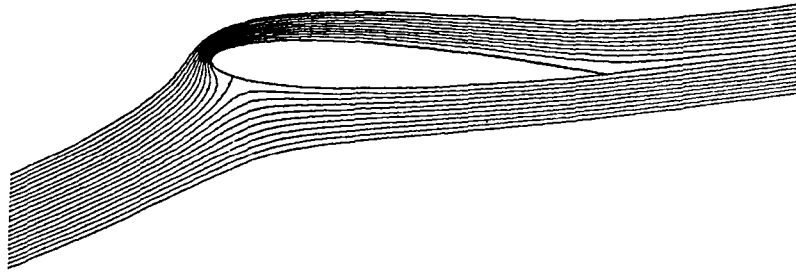


Figure 14. - Streamlines around the NACA 0012 airfoil:
 $Re = 2.88 \times 10^6$, $\alpha = 16^\circ$ and $M_\infty = 0.1$.

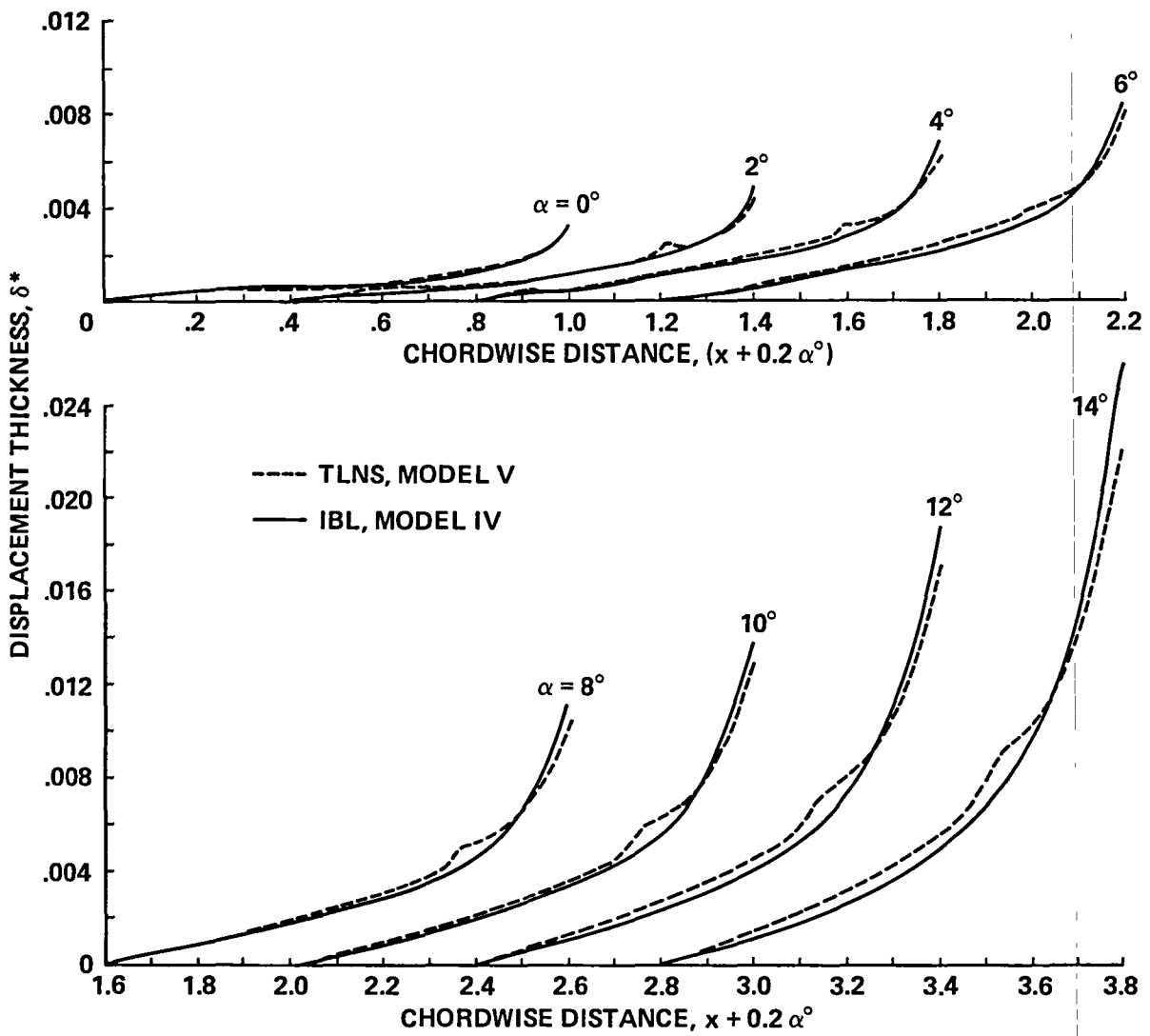


Figure 15. - Comparison of displacement thickness distributions:
 NACA 0012, $Re = 2.88 \times 10^6$.

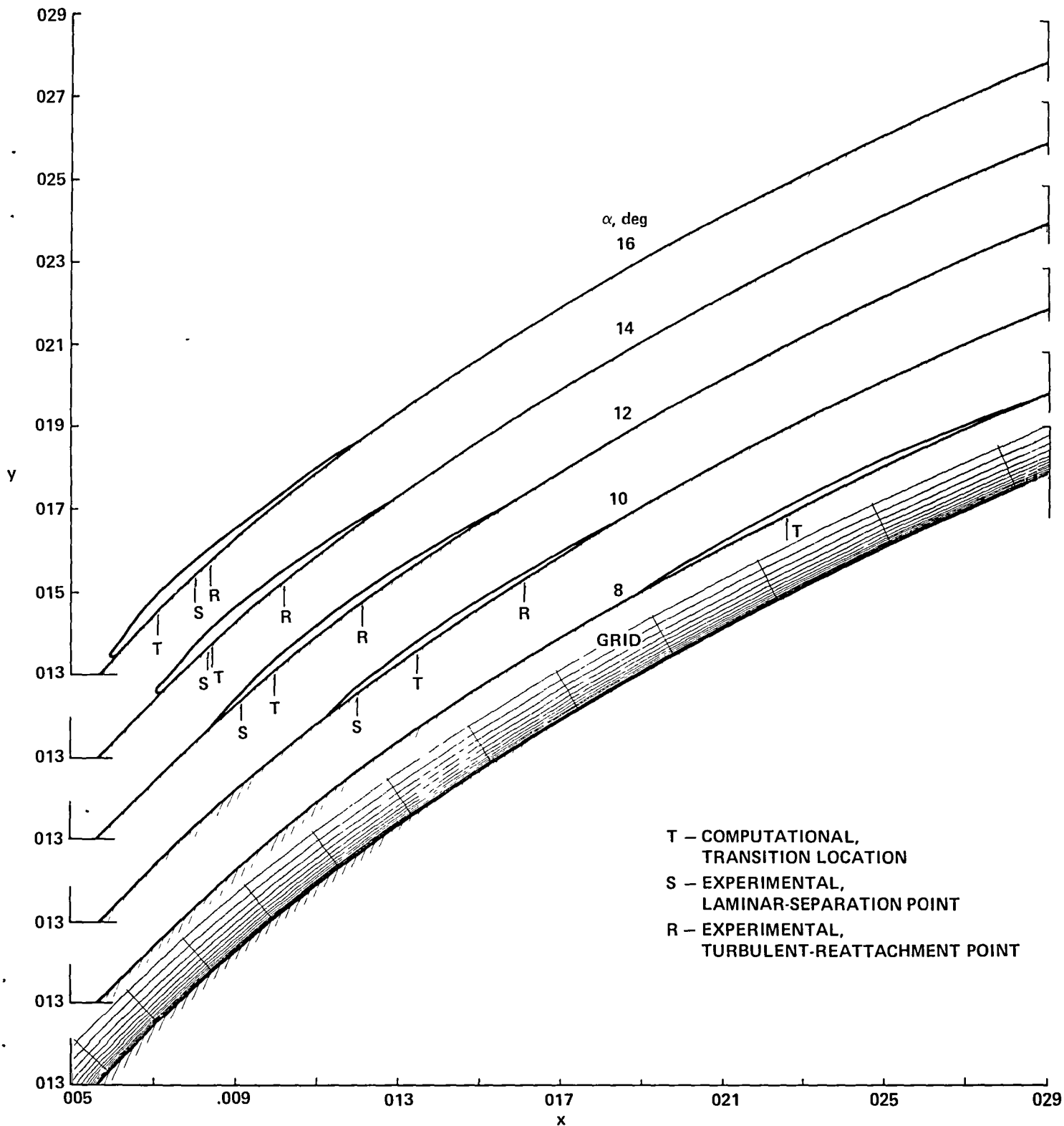


Figure 16. - Transitional-separation bubbles determined with the TLNS method and Model V on the NACA 0012 airfoil: $Re = 2.88 \times 10^6$ and $M_\infty = 0.1$.

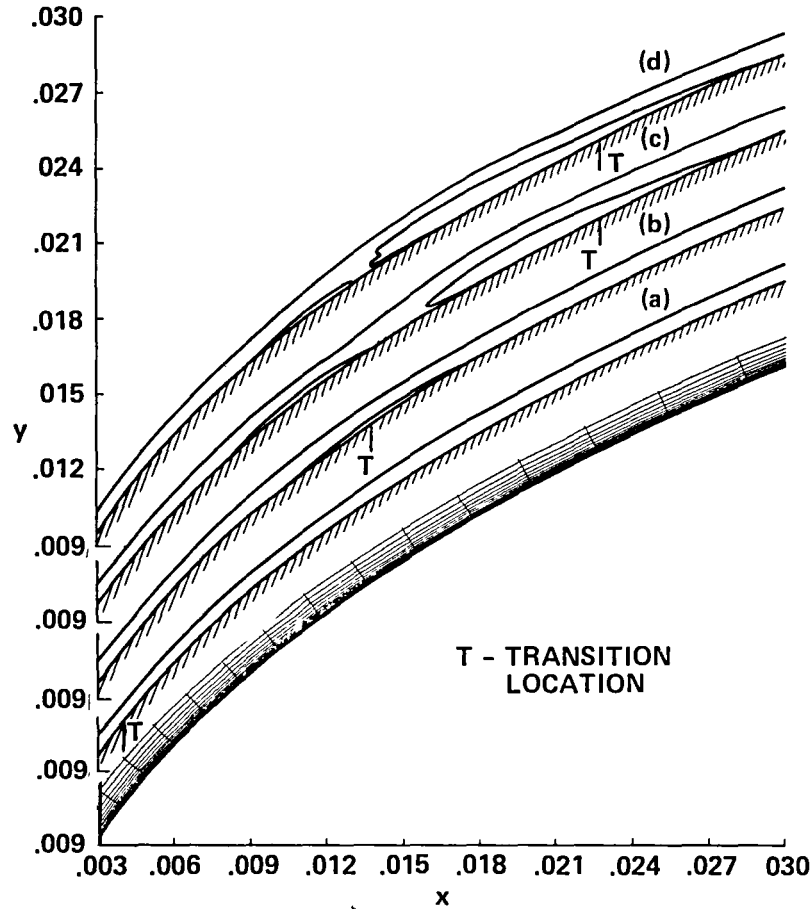


Figure 17. - Effect of transition location on transitional-separation bubbles:
 $Re = 2.88 \times 10^6$, $M_\infty = 0.1$, $\alpha = 10^\circ$.

With s as the streamwise coordinate, a shear layer, whose thickness is δ at a distance L from its origin, is considered to be thin if $\partial\delta/\partial s$ is of order δ/L and is much smaller than unity, that is, if $\partial\delta/\partial s \ll 1$. Note that it is the local rate of change that matters. In this case, the Navier-Stokes equations reduce to the boundary-layer equations. These latter equations are useful only if they are in a coordinate system such that s is in the direction of the thin shear layer. When this thin-shear-layer approximation is applicable, the ratio of neglected to retained stress gradients is $O[(\partial\delta/\partial s)^2]$ for laminar flows and $O(\partial\delta/\partial s)$ for turbulent flows. Since $(\partial\delta/\partial s)$ is generally larger in turbulent flows than in laminar flows, this approximation is less accurate in turbulent flows. Typically, the neglected streamwise viscous diffusion and turbulent diffusion are, respectively, $O(5.3Re^{-1})$ and $O(0.37Re^{-1/5})$ for $Re \leq 10^7$.

The upstream influence is provided by the pressure field in subsonic regions, by transport of momentum in the upstream direction in separated flows, and by streamwise gradients of viscous and turbulence stresses, as indicated by the direction of the arrows in figure 23. The first or the last of these influences makes the flow field and the governing equations elliptic in the spatial dimensions. The correction owing to the displacement effect can indirectly transmit the upstream influence of the pressure field via the external flow, but not through the shear layer. A correction owing to displacement thickness in the "inviscid" flow at a station leads to a correction in the

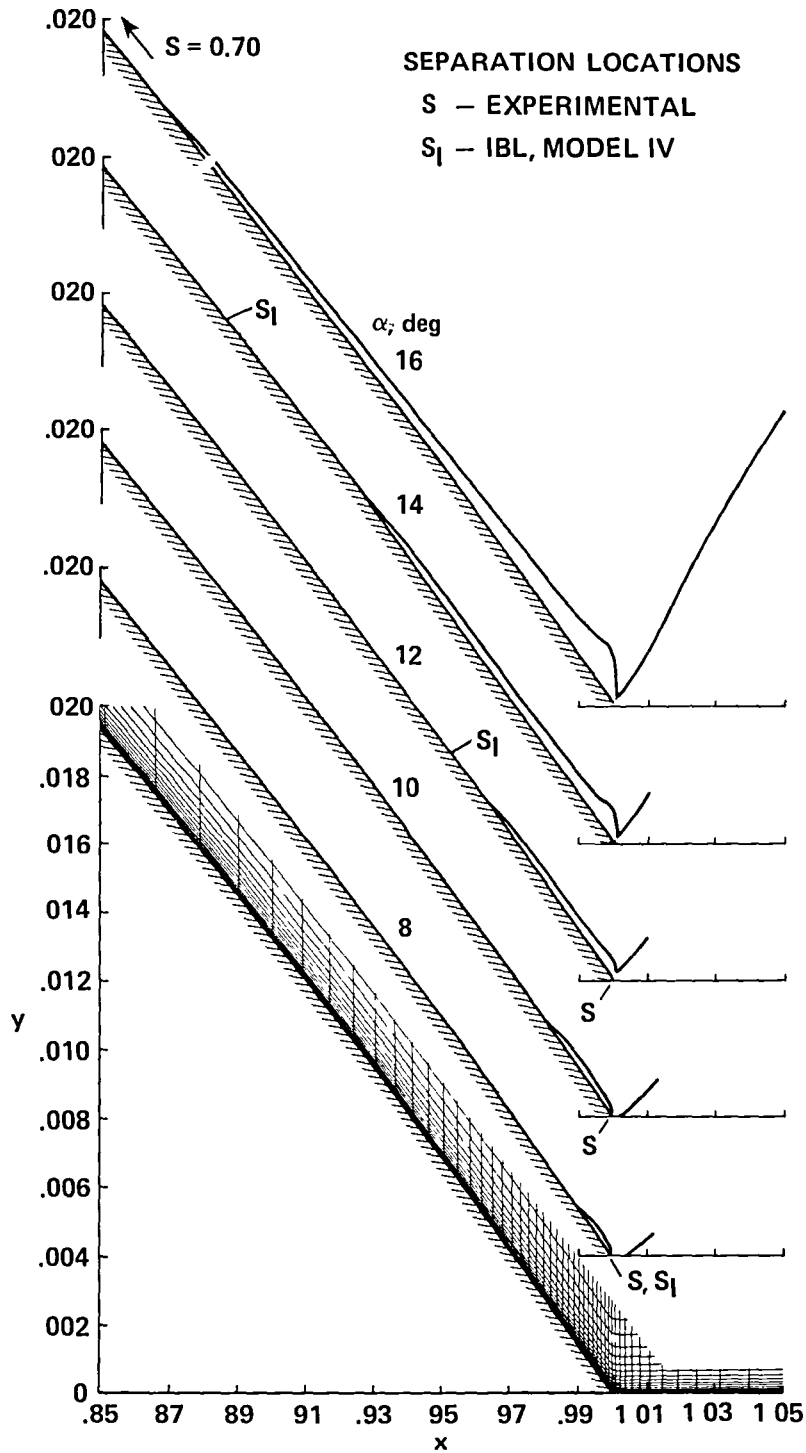
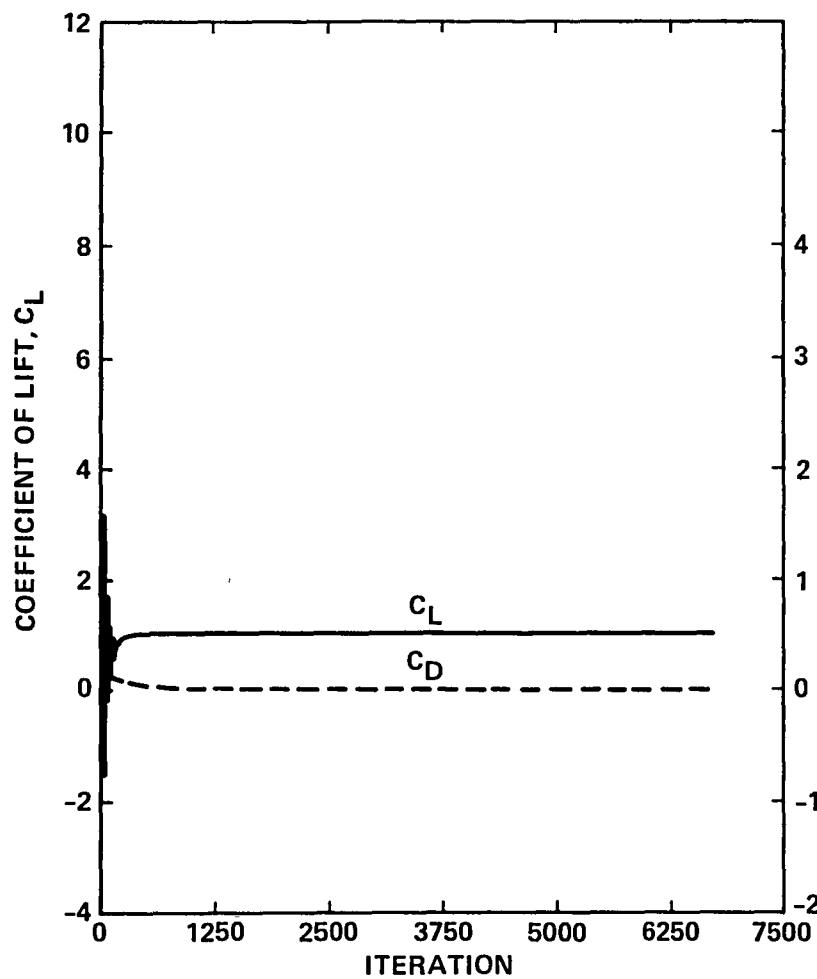
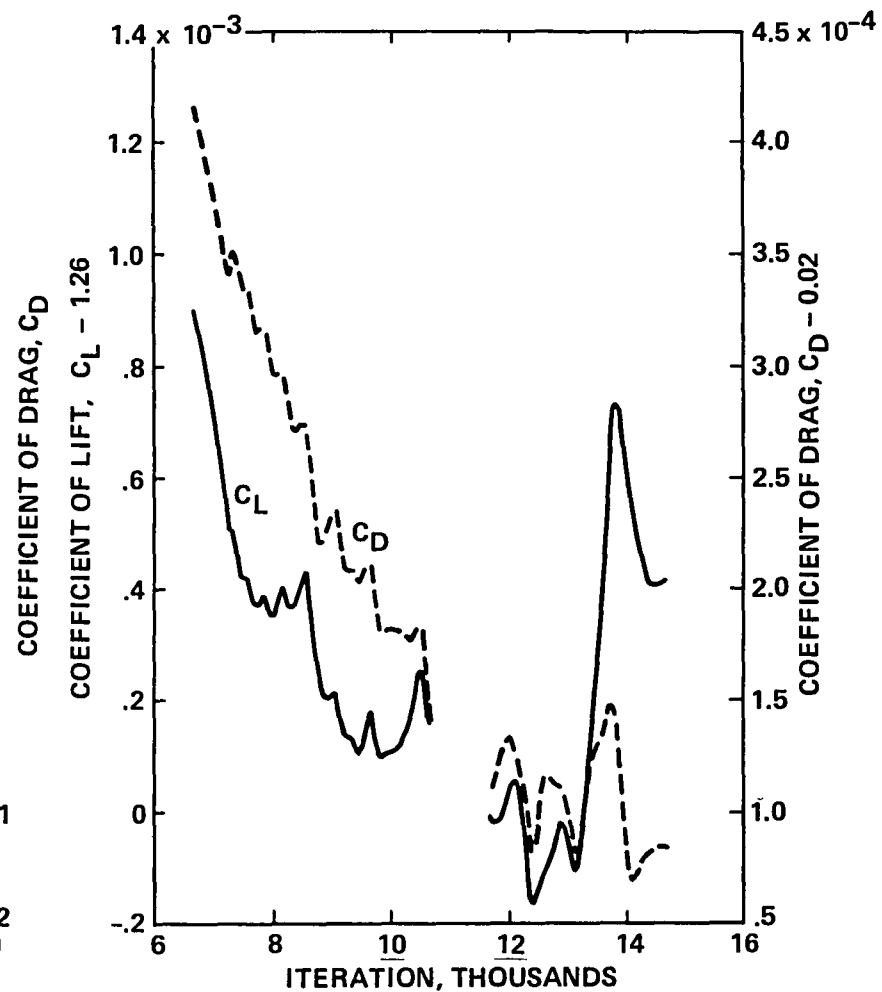


Figure 18. - Turbulent separated regions obtained with the TLNS method and Model V on the NACA 0012 airfoil: $Re = 2.88 \times 10^6$ and $M_\infty = 0.1$.

pressure distribution upstream of this station. This procedure is a part of the IBL theory. On the other hand, the correction owing to curvature effect accounts for the variation of the pressure



(a)



(b)

Figure 19. - Convergence histories for lift and drag coefficients:
 $Re = 3.0 \times 10^6$, $\alpha = 12^\circ$, and $M_\infty = 0.1$.

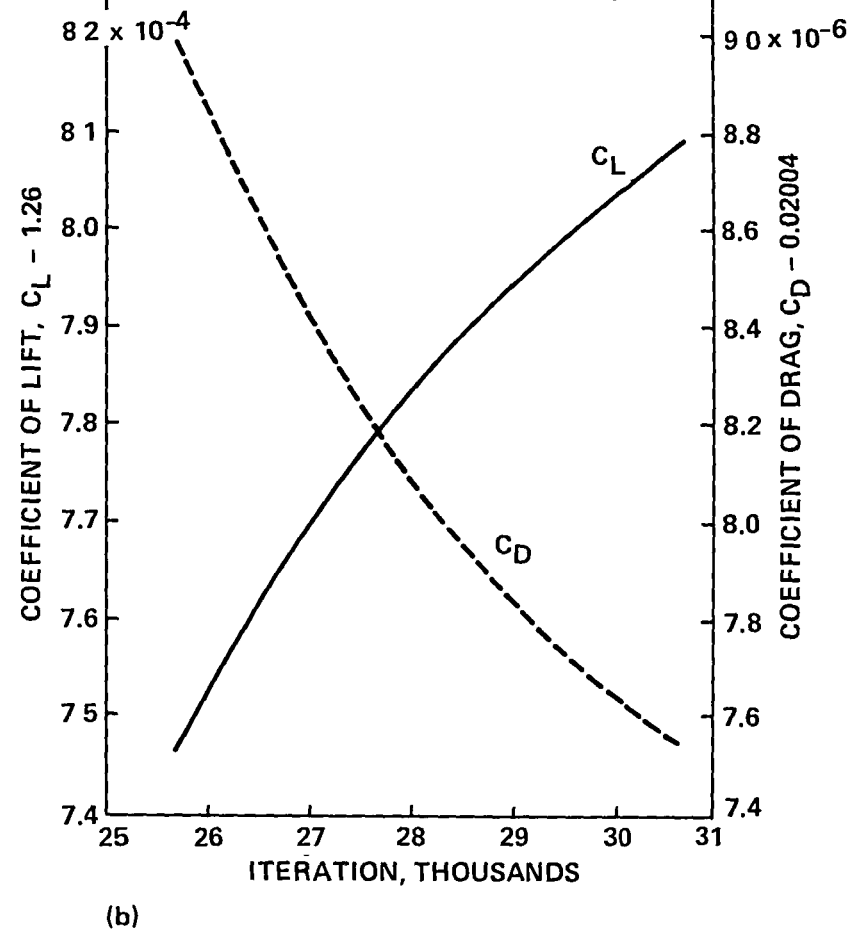
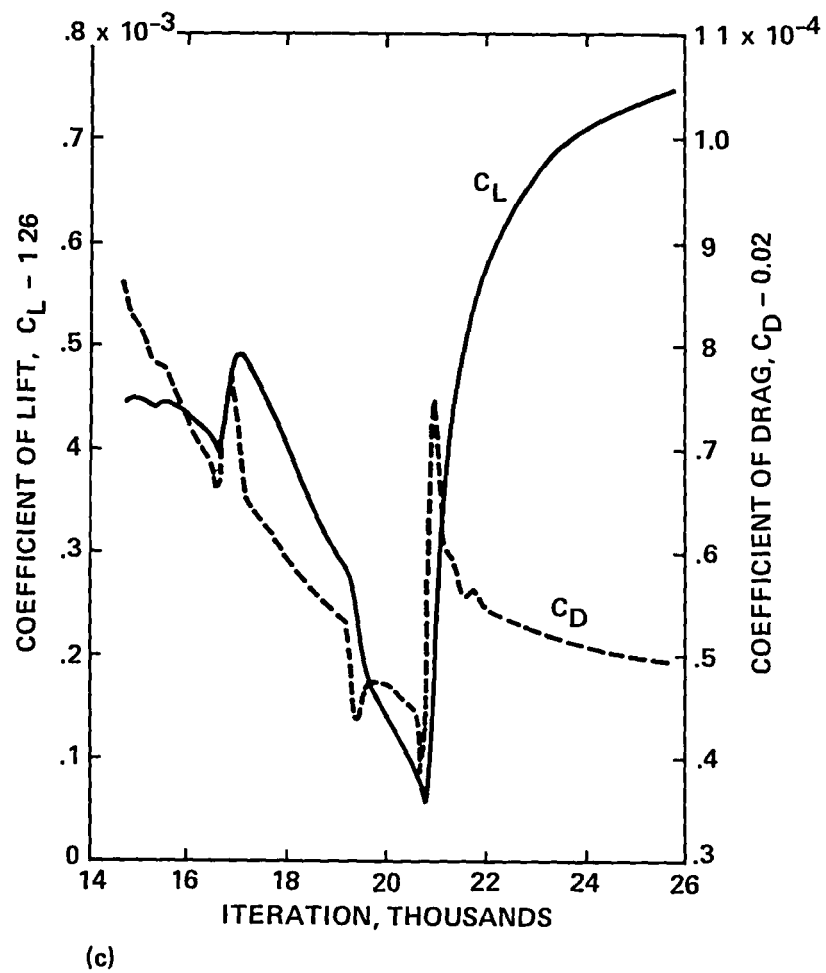


Figure 19 - Concluded.

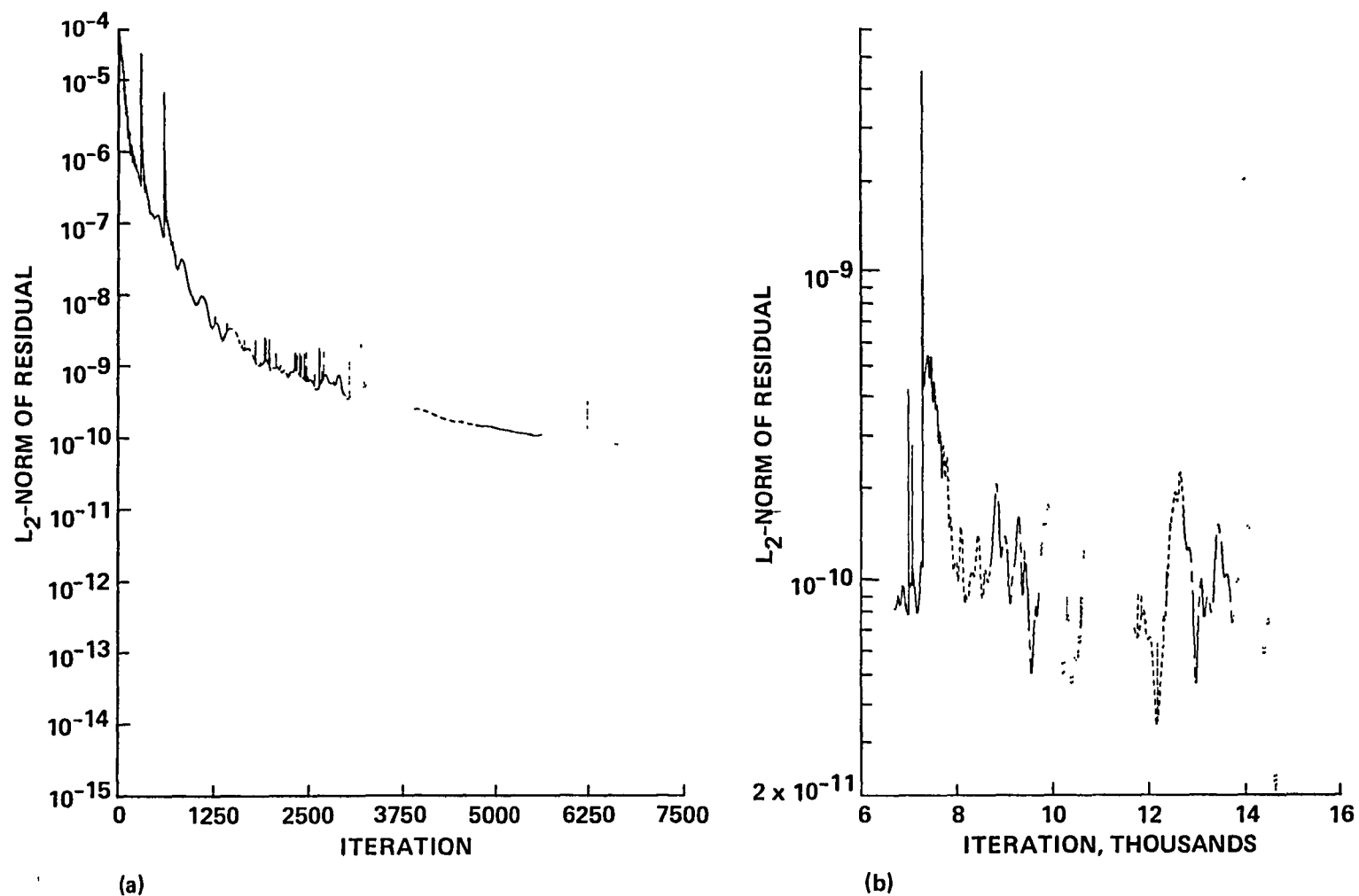


Figure 20. - Convergence history for mass conservation equation:
 $Re = 3.0 \times 10^6$, $\alpha = 12^\circ$, and $M_\infty = 0.1$.

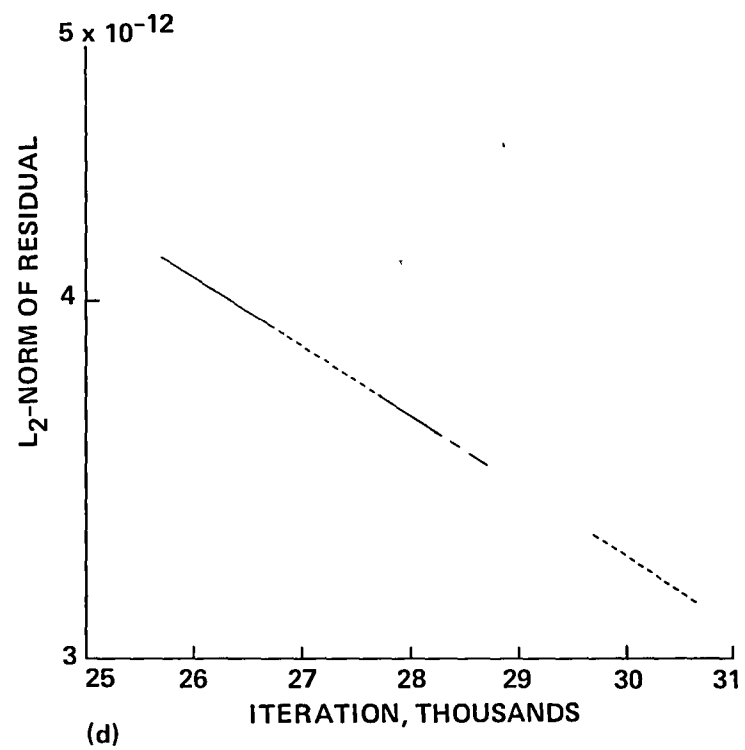
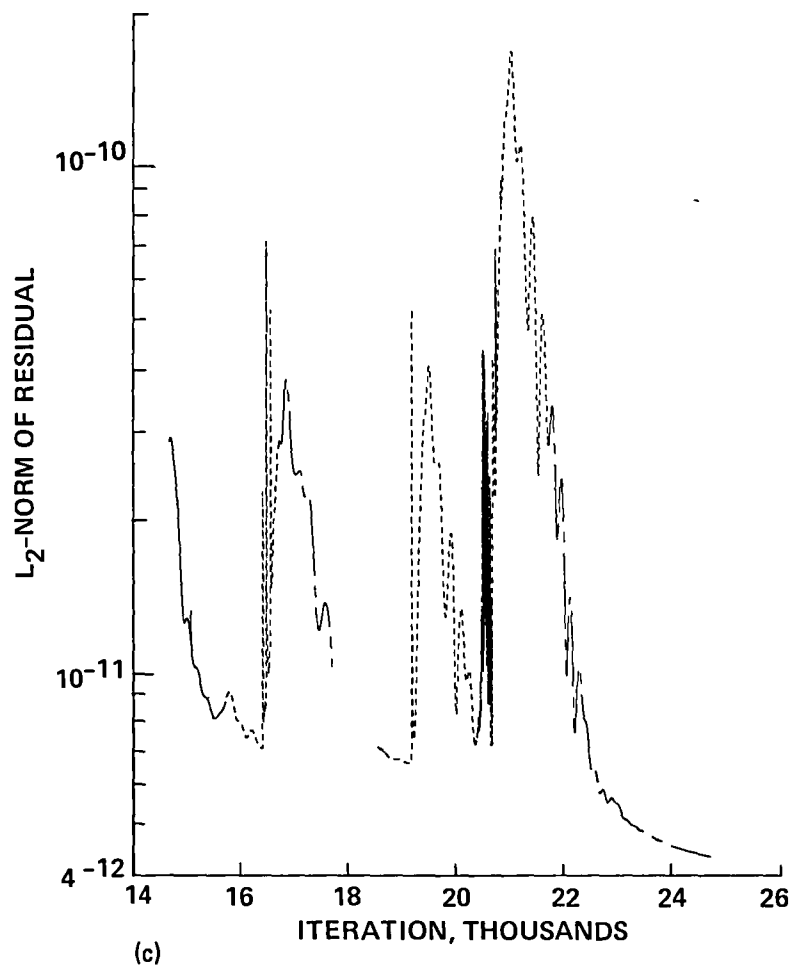


Figure 20. - Concluded.

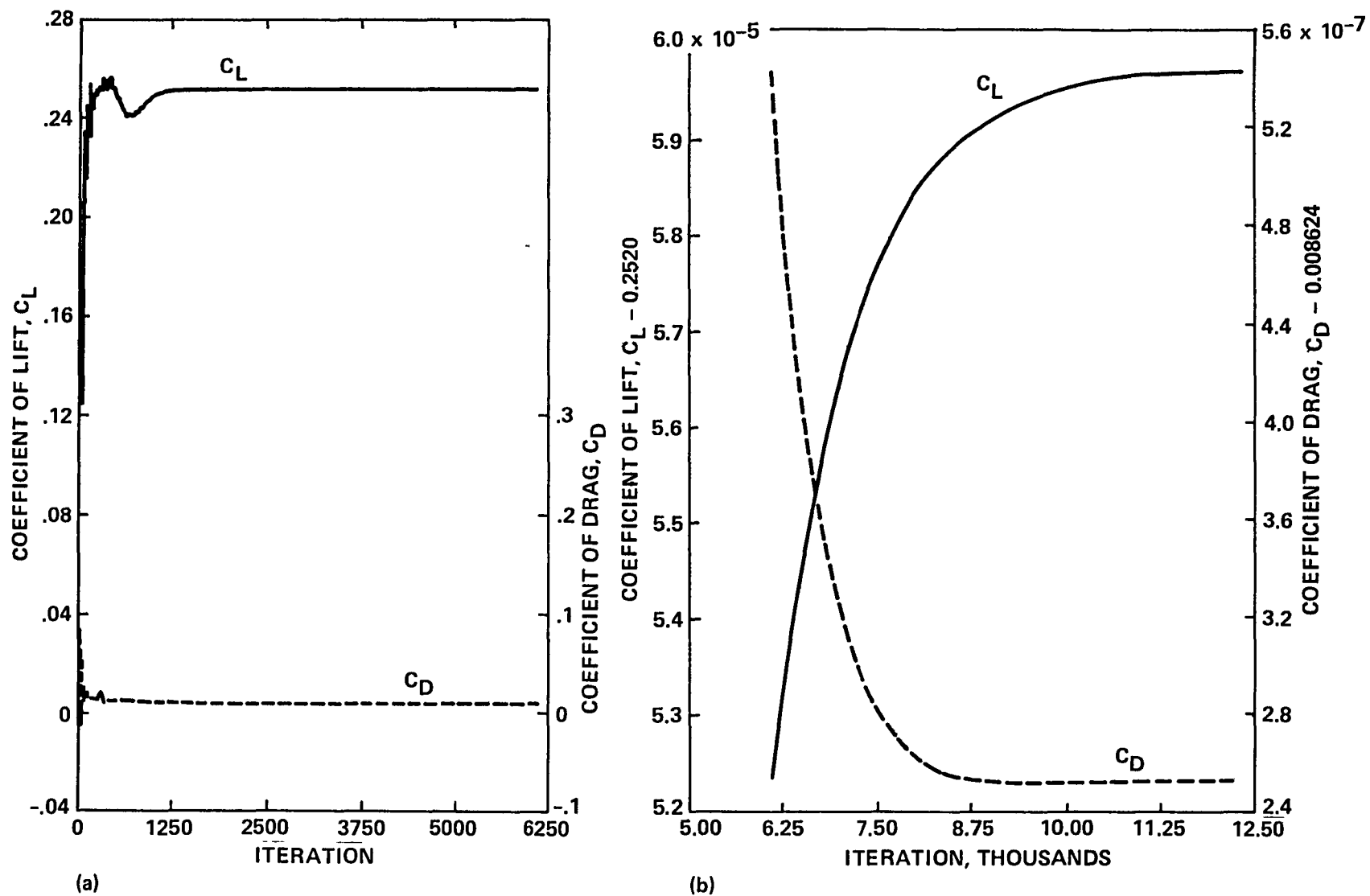


Figure 21. - Convergence histories for lift and drag coefficients:
 $Re = 6.0 \times 10^6$, $\alpha = 2^\circ$, and $M_\infty = 0.5$.

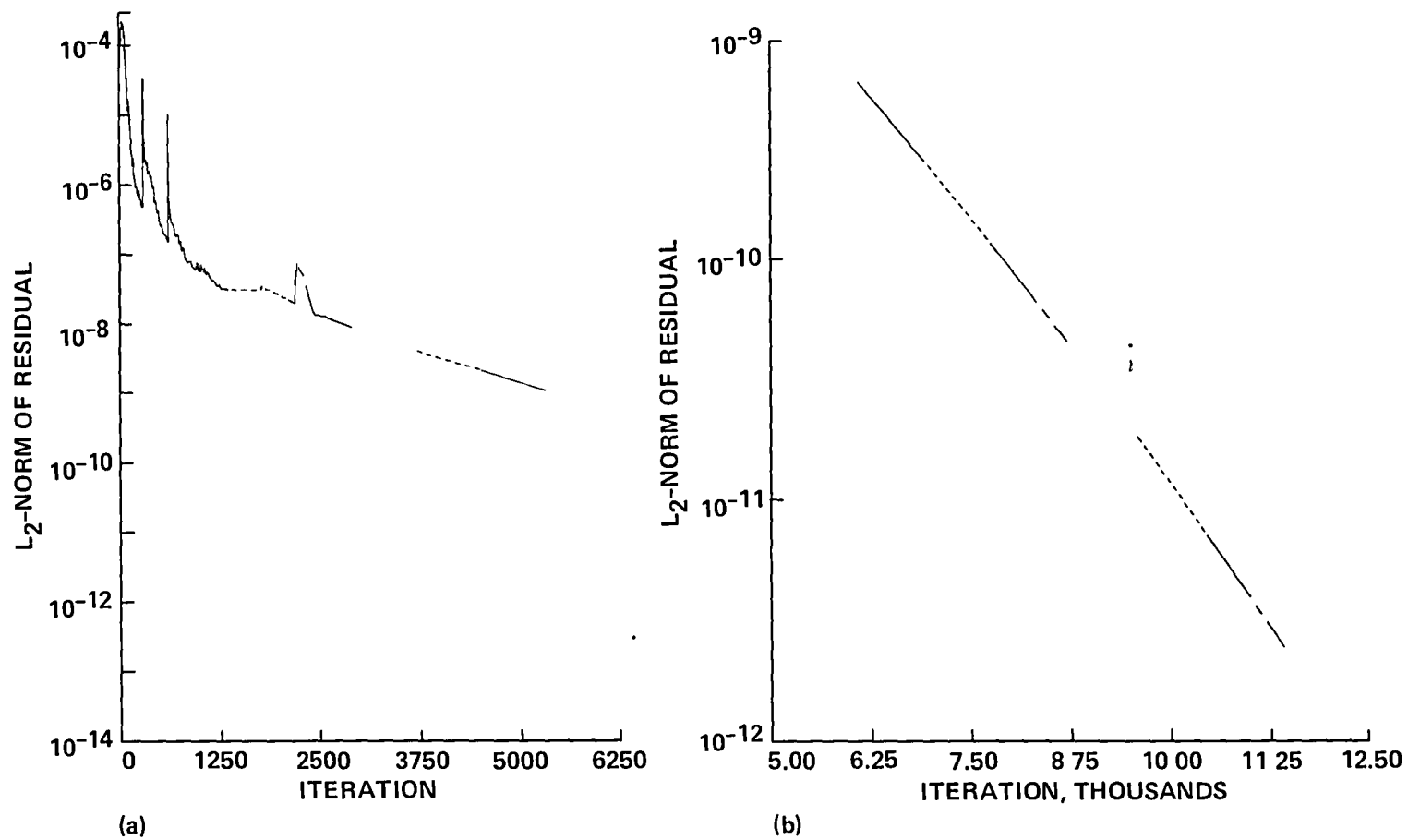


Figure 22. - Convergence history for mass conservation equation:
 $Re = 6.0 \times 10^6$, $\alpha = 2^\circ$, and $M_\infty = 0.5$.

field across the shear layer, but not for the upstream influence of this field through this layer. In addition, this correction is limited to shear layers that are thin, since the curvature of streamline varies substantially across thick shear layers. Usually, in high- Re , laminar separated flows there is significant upstream influence of the velocity field relative to that of the pressure field within the shear layer so that the latter can be neglected. The boundary-layer theory does not account for the upstream influence of streamwise gradients of viscous and turbulence stresses. These stresses are generally negligible at normal (high) Reynolds numbers.

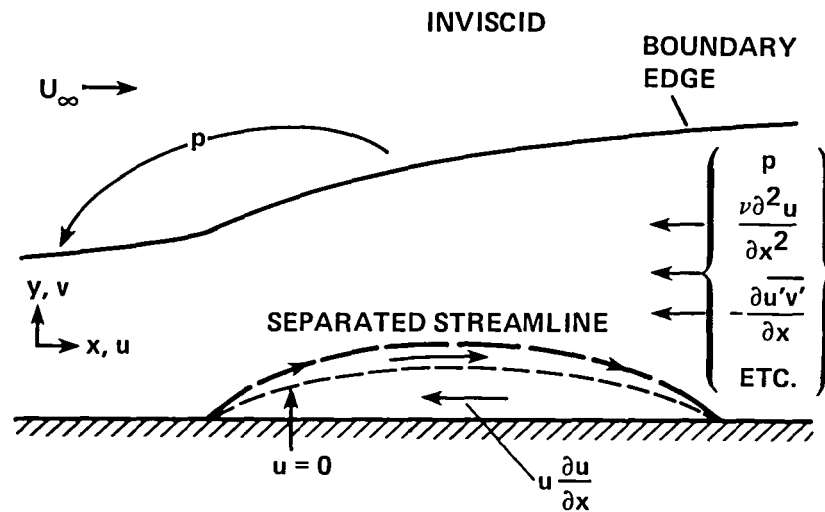


Figure 23. - Upstream influences. (From ref. 33.)

The main difference between the present IBL procedure and the TLNS procedure is identified by considering what upstream influences these procedures account for. Neither handles the upstream influence of viscous and turbulent stresses. Both handle the upstream transfer of momentum. The difference between these procedures arises when the upstream influence of the pressure field is dealt with. In order to explain this, the upstream influence of the pressure field is broken up into two parts: one through the shear layer and the other through the inviscid region. The TLNS formulation accounts for both of these parts; but the IBL formulation accounts only for the second part, through the consideration of the displacement thickness. This is the fundamental difference between these two formulations.

When a shear layer is neither thin nor slender, the Navier-stokes equations are necessary. The upstream influence of both the pressure field and streamwise gradients of viscous and turbulent stresses are then important. The upstream influence of the pressure field is much more pronounced than in a thin shear layer, owing to significant normal pressure gradients; for example, in large separated regions, in the trailing-edge region of an airfoil, and in interactions of a shock wave and a boundary layer. Further, the streamwise gradients of stresses cannot be neglected, for example, in low-Reynolds-number flows and when the velocity field encounters rapid variations in streamwise direction, such as flow past the trailing edge of an airfoil, across a shock wave within a boundary layer, and around a point of flow separation. It remains to establish the magnitude and

significance of error introduced by the IBL approach vis-à-vis the TLNS approach in the above situations that are of relevance in high-speed aerodynamics.

CONCLUDING REMARKS

Numerical procedures for the solution of the TLNS equations and for the interaction of solutions to inviscid and boundary-layer equations were described and evaluated. To allow appraisal of the numerical and fluid dynamic abilities of the two schemes, they were applied to one airfoil over a range of angles of attack. Calculations were performed with algebraic eddy-viscosity formulations, and consideration of transition was included. In general, the IBL procedure is computationally efficient but theoretically restrictive relative to the TLNS procedure.

Some specific conclusions can easily be extracted from the preceding section. It is clear, for example, that both procedures will allow the calculation of lift coefficient with acceptable accuracy at angles of attack that cover laminar separation bubbles but that fall short of C_{Lmax} . The TLNS procedure appears to better predict drag than the IBL procedure. The latter procedure can be improved by including the cross-stream pressure gradient, and the wake streamline curvature effect to better predict the drag force.

Based on the TLNS results, the far-field wake turbulence model seems to have negligible effect on the loads acting on the airfoil. In common with the findings of references 6 and 34, the calculations of pressure and lift confirm that the algebraic eddy-viscosity formulations adequately represent the boundary-layer flows and the wake up to angles of attack close to that of C_{Lmax} , as long as the turbulent separated region is thin.

The location of transition is crucial. Either some significant feature may be missing in a computation or an iterative procedure may not converge, depending on whether the location in the computation is upstream or downstream of that feature in reality. Further work is necessary to determine the role of transition at high angles of attack, and to confirm and extend this report and the reports of Cebeci et al. (ref. 1) and of Carr and Cebeci (ref. 31) concerning the influence of the transition location on the flow properties and the break down of calculation procedure.

The studies in reference 1 indicate that the shape of the airfoil also plays an important role in calculating its lift and drag coefficients. Additional calculations, similar to those discussed in this paper for a symmetrical airfoil, should be performed for cambered and supercritical airfoils.

When the upstream influence of pressure field *through* the shear layer is important, the TLNS procedure has an edge over the IBL. There is no doubt that the TLNS equations are more general than those associated with the IBL procedure, even if the IBL equations are modified to include the cross-stream pressure gradient. On the other hand, the cost of using the computer program that embodies the TLNS equations is considerably greater than that of the program that embodies the IBL equations. This cost may limit the use of the TLNS equations in a design cycle with presently available computing power even for two-dimensional flows. Therefore, it is necessary to improve the numerical algorithm of the Navier-Stokes procedure and, in the meantime, to attempt to establish those flows for which its added generality is required.

APPENDIX

THE TLNS METHOD

The derivation of the approximate-factorization scheme presented below is different from that given by Beam and Warming (ref. 3) for the Navier-Stokes equations in Cartesian coordinates and extended by Steger (ref. 4) for these equations in curvilinear coordinates. The steps involved in formulating the present scheme are as follows. First, the governing equation is evaluated at a new or unknown time-level $(n + 1)$ and the time-derivative is approximated by a backward difference formula. Second, assuming that the effective viscosity and thermal conductivity are not functions of time, the spatial derivatives at the $(n + 1)$ level are expressed by a Taylor series expansion in terms of known quantities at the (n) level, and of time-derivatives of dependent variables at the $(n + 1)$ level. This leads to linearization of the nonlinear terms in governing equations. The Jacobian and metric coefficients of spatial coordinates and the time-variable are considered to be known at the $(n + 1)$ level. Third, the left-hand side of the equation resulting from the previous step is approximately factored to form an ADI procedure. Fourth, the continuous space derivatives are replaced by finite differences. Fifth, numerical dissipation is added in the numerical procedure. Sixth, physical and analytical boundary conditions are translated into finite-difference boundary conditions. Instead of formulating these boundary conditions implicitly and incorporating them in the ADI procedure, boundary values of the dependent variables are determined using the previous time-step solution. Seventh, the solution of the equation formed in the fifth step determines the time-derivative of the dependent variable at the $(n + 1)$ level. This time-derivative then is replaced by a backward finite-difference formula in order to determine the dependent variable at the $(n + 1)$ level.

The above steps are explained below in detail for the thin-layer Navier-Stokes equations. Note that the derivation of the approximate factorization scheme for the Navier-Stokes equations follow the same steps.

Linearization and Approximate Factorization

The nondimensional form of the TLNS equations are written in the following form:

$$\frac{\partial Q_m}{\partial \tau} = \mathfrak{R}_m \quad (22)$$

with

$$\mathfrak{R}_m \equiv - \sum_{i=1}^2 \frac{\partial C_{m_i}}{\partial \xi_i} + \frac{1}{Re} \frac{\partial \mathcal{V}_m^*}{\partial \xi_2}$$

where

$$\mathcal{V}_m^* = \sum_{i=1}^2 \left(\rho \mathcal{V}_{m_i} \frac{\partial \xi_2}{\partial x_i} \right)$$

The Cartesian, conservative dependent variables, convective and pressure terms, and diffusive terms are associated with Q_m , C_{m_i} , and \mathcal{V}_m^* , respectively. The Jacobian of transformation from the Cartesian coordinates x_i to curvilinear coordinates ξ_i is denoted by \mathcal{D} . The subscript m is the equation number, varying from 1 to 4.

Let the numerical solution of equation (22) with appropriate boundary and initial conditions be known at time-level (n). The numerical solution of this equation is required at time-level ($n+1$) by using an implicit scheme. Therefore, this equation is evaluated at the ($n+1$) time-level, and the time-derivative is replaced by a backward difference formula,

$$\left(\frac{\partial Q_m}{\partial \tau}\right)^{(n+1)} = \left(\frac{\delta Q_m}{\delta \tau}\right)^{(n+1)} + \mathcal{O}(\Delta \tau^p) \quad (23)$$

where δ is a backward finite-difference operator that is not of the Padé type. This backward difference formula is not presented at this point because it is not required in the next few steps. It is defined in the seventh step below along with the value of p .

After substituting formula (23) for the time-derivative in equation (22), we have

$$\left(\frac{\delta Q_m}{\delta \tau}\right)^{(n+1)} = \mathfrak{R}_m^{(n+1)} + \mathcal{O}(\Delta \tau^p) \quad (24)$$

We have unknown quantities on both side of equation (24), making this equation and the numerical algorithm developed below implicit.

The terms represented by $\mathfrak{R}_m^{(n+1)}$ on the right-hand side of equation (24) are expanded in a Taylor series of time τ . The expansion of C_{m_i} -term is

$$\begin{aligned} \left(\sum_{i=1}^2 \frac{\partial C_{m_i}}{\partial \xi_i}\right)^{(n+1)} &= \sum_{i=1}^2 \left(\frac{\partial C_{m_i}}{\partial \xi_i}\right)^{(n)} + \sum_{i=1}^2 \left\{ \Delta \tau \frac{\partial}{\partial \xi_i} \left[\sum_{k=1}^4 \left(\frac{\partial C_{k_i}}{\partial Q_k}\right)^{(n)} \left(\frac{\delta Q_m}{\delta \tau}\right)^{(n+1)} \right] \right\} \\ &+ \mathcal{O}(\Delta \tau^2) + \mathcal{O}(\Delta \tau^{p+1}) \end{aligned} \quad (25)$$

where

$$\left(\frac{\partial Q_m}{\partial \tau}\right)^{(n)} = \left(\frac{\partial Q_m}{\partial \tau}\right)^{(n+1)} + \mathcal{O}(\Delta \tau) \quad (26)$$

and equation (23) are used. The vector \mathcal{V}_m^* of the viscous term contains first derivatives. These are derivatives of functions that are of the form $\beta = \beta(Q)$. Symbolically, this is written as $\mathcal{V}_m^* = \mathcal{V}_m^*(\beta_1, \beta_2, \dots) = \mathcal{V}_m^*(\beta)$. Instead of expanding directly (ref. 3) \mathcal{V}_m^* in a Taylor series, it is indirectly expanded by writing each β in a Taylor series:

$$\beta^{n+1} = \beta^{(n)} + \Delta \tau \sum_{m=1}^4 \left(\frac{\partial \beta}{\partial Q_m}\right)^{(n)} \left(\frac{\delta Q_m}{\delta \tau}\right)^{(n+1)} + \mathcal{O}(\Delta \tau^2) + \mathcal{O}[\Delta \tau^{p+1}] \quad (27)$$

The viscous term at the ($n+1$) level is the expressed as

$$\left(\frac{\partial \mathcal{V}_m^*(\beta)}{\partial \xi_2}\right)^{(n+1)} = \left\{ \left[\frac{\partial \mathcal{V}_m^*(\beta)}{\partial \xi_2}\right]^{(n)} + \Delta \tau \frac{\partial \mathcal{V}_m^*(\epsilon^{(n+1)})}{\partial \xi_2} \right\} + \mathcal{O}(\Delta \tau^2) + \mathcal{O}[\Delta \tau^{p+1}] \quad (28)$$

where

$$\epsilon^{(n+1)} = \sum_{m=1}^4 \left(\frac{\partial \beta}{\partial Q_m} \right)^{(n)} \left(\frac{\delta Q_m}{\delta t} \right)^{(n+1)}$$

By using equations (25) and (28), we can reformulate equation (24) to

$$\begin{aligned} \left(\frac{\delta Q_m}{\delta \tau} \right)^{(n+1)} + \Delta \tau \left\{ \sum_{i=1}^2 \frac{\partial}{\partial \xi_i} \left[\sum_{k=1}^4 \left(\frac{\partial C_{ki}}{\partial Q_k} \right)^{(n)} \left(\frac{\delta Q_m}{\delta t} \right)^{(n+1)} \right] - \frac{\partial \mathcal{V}_m^*(\epsilon^{(n+1)})}{\partial \xi_2} \right\} \\ = \mathfrak{R}_m^{*(n)} + \mathcal{O}(\Delta \tau^2) + \mathcal{O}[\Delta \tau^p] \end{aligned} \quad (29)$$

where the Jacobian and metric coefficients are evaluated at the $(n+1)$ time-level in $\mathfrak{R}_m^{*(n)}$. This is the only difference between this latter quantity and $\mathfrak{R}_m^{(n)}$. The approximate factoring of the left-hand side of the above equation and the omission of the truncation error on the right-hand side lead to the following alternating direction algorithm in “derivative” form:

$$\left(\frac{\delta Q_m}{\delta \tau} \right)^I + \Delta \tau \left\{ \frac{\partial}{\partial \xi_2} \left[\sum_{k=1}^4 \left(\frac{\partial C_{k2}}{\partial Q_k} \right)^{(n)} \left(\frac{\delta Q_m}{\delta \tau} \right)^I \right] - \frac{\partial \mathcal{V}_m^*(\epsilon^{(I)})}{\partial \xi_2} \right\} = \mathfrak{R}_m^{*(n)} \quad (30)$$

$$\left(\frac{\delta Q_m}{\delta \tau} \right)^{(n+1)} + \Delta \tau \frac{\partial}{\partial \xi_1} \left[\sum_{k=1}^4 \left(\frac{\partial C_{k1}}{\partial Q_k} \right)^{(n)} \left(\frac{\delta Q_m}{\delta t} \right)^{(n+1)} \right] = \left(\frac{\delta Q_m}{\delta \tau} \right)^I \quad (31)$$

with a factorization error $\mathcal{O}(\Delta \tau^2)$. The first factor is in the ξ_2 -direction rather than in the ξ_1 -direction so that the effect of the boundary conditions is transmitted quickly from the surface of the airfoil to the interior of the flow field. The Roman numerals are used to indicate dummy time-derivatives.

Numerical Dissipation

Minimum numerical dissipation is used so that stable numerical solutions are obtained in reasonable amount of computer time. The added dissipation is patterned after that developed by Jameson et al. (ref. 12). The form of this dissipation and the various constants appearing in it are kept the same for all cases. The numerical dissipation D_m is given by

$$D_m = - \sum_{i=1}^2 \varrho_i \frac{Q_{mi}}{\mathcal{D}} \quad (32)$$

with

$$\varrho_a \equiv \left(\frac{\Delta \xi_a^4 \varepsilon_a}{64 \Delta \tau} \right) \frac{\partial}{\partial \xi_a} \left(\varphi_a \frac{\partial^3}{\partial \xi_a^3} \right)$$

where $\varphi_a = \sigma_{\xi_a} \mathcal{D}$. The subscript a is either 1 or 2. In the present study, ε_1 and ε_2 are, respectively, 0.64 and 0.07. The term σ_{ξ_i} is defined as

$$\sigma_{\xi_i} = \left\{ |\mathcal{U}_1| + a \left[\left(\frac{\partial \xi_1}{\partial x_1} \right)^2 + \left(\frac{\partial \xi_1}{\partial x_2} \right)^2 \right]^{1/2} \right\}, \quad \sigma_{\xi_2} = c \quad (33)$$

where \mathcal{U} and a are the contravariant velocity and the speed of sound, respectively, and where the constant $c = 64$. Equation (33) was specifically formulated for the present study. Observe that the numerical dissipation in the ξ_2 -direction, the direction in which viscous and turbulent stresses are dominant, is much less than that in the other direction.

The above fourth-order dissipative term damps the short wavelength ($2\Delta\xi_i$) oscillations. Since it is of higher order than the second-order-accurate central differences, it does not disrupt the formal accuracy of the numerical scheme. Although numerical dissipation is not, in conventional terminology, part of the turbulence model, it is in practice. Consequently, the analytical form of the turbulence model is not sufficient to describe its effect on an actual calculation. The numerical turbulence model includes the internal logic controlling the local evaluation of parameters such as mixing length, the discretization error, and the numerical dissipation (ref. 8). It seems that the only way the effect of numerics can be separated from the analytical turbulence model is by grid-refinement studies leading to elimination of numerical dissipation. In the absence of this, the final judgment of the computed results is generally based on a comparison with some experiment or theory.

The numerical dissipation given in equation (32) is treated the same as the right-hand side of equation (22). This leads to linearization of D_m resulting into two terms, one on either side of equation (29). Without the truncation error, this equation becomes

$$\begin{aligned} \left(\frac{\delta Q_m}{\delta \tau}\right)^{(n+1)} + \Delta\tau \left\{ \sum_{i=1}^2 \frac{\partial}{\partial \xi_i} \left[\sum_{k=1}^4 \left(\frac{\partial C_{ki}}{\partial Q_k}\right)^{(n)} \left(\frac{\delta Q_m}{\delta t}\right)^{(n+1)} \right] - \frac{\partial \mathcal{V}_m^*(\epsilon^{(n+1)})}{\partial \xi_2} \right\} \\ + \Delta\tau \sum_{i=1}^2 \varrho_i \left(\frac{1}{\mathcal{D}} \frac{\delta Q_{mi}}{\delta \tau} \right)^{(n+1)} \\ = \mathfrak{R}_m^{*(n)} - D_m^{*(n)} \end{aligned} \quad (34)$$

where

$$D_m^{*(n)} = - \sum_{i=1}^2 \varrho_i \left(\frac{Q_{mi}^{(n)}}{\mathcal{D}^{(n+1)}} \right)$$

The variable σ_{ξ_1} is assumed to be time-independent because its linearization produces terms that are difficult to handle and time consuming. The approximately factored form of equation (34) leads to pentadiagonal-block systems.

Spatial Differencing

Except for the viscous terms, the spatial derivatives appearing in equation (34) are approximated by three-point central-difference approximations in the interior of the computational domain. At the boundaries, the metric coefficients are evaluated using two-point sided-differences. Vorticity and effective viscosity are computed at the grid-point location of the mesh system.

The evaluation of the viscous terms requires a special treatment because the effective viscosity is a function of spatial coordinates. The form of a typical viscous term and, for example, its

second-order finite-difference form (ref. 4), are as follows:

$$\frac{\partial}{\partial \xi} \left(\mu \frac{\partial f}{\partial \xi} \right) = \frac{[\mu_{(j-1)} + \mu_{(j)}] f_{(j-1)} - [\mu_{(j+1)} + 2\mu_{(j)} + \mu_{(j-1)}] f_{(j)} + [\mu_{(j)} + \mu_{(j+1)}] f_{(j+1)}}{2\Delta \xi^2} + O(\Delta \xi^2) \quad (35)$$

Here, the subscript indices denote grid-point locations either in the ξ_1 - or ξ_2 -direction.

The fourth derivatives in the dissipative terms are evaluated as follows

$$\frac{\partial}{\partial \xi_a} \left(\varphi_a \frac{\partial^3 (Q_m/D)}{\partial \xi_a^3} \right)_{(j)} = \nabla_{\xi_a} \varphi_{a(j)} (\Delta_{\xi_a} \nabla_{\xi_a} \Delta_{\xi_a} Q_{m(j)}) \quad (36)$$

where the various operators are defined as

$$\begin{aligned} \varphi_{a(j)} &\equiv (\sigma_{\xi_a(j+1)} D_{(j+1)} + \sigma_{\xi_a(j)} D_{(j)}) \\ \nabla_{\xi_a} Q_{m(j)} &\equiv Q_{m(j)} - Q_{m(j-1)} \\ \Delta_{\xi_a} Q_{m(j)} &\equiv Q_{m(j+1)} - Q_{m(j)} \end{aligned}$$

Boundary Conditions

Boundary conditions for the equations of motion are determined by mathematical and physical considerations (ref. 8). The mathematical character of these governing equations dictates the number and type of boundary conditions that determine, along with initial conditions, the well-posedness of a problem, that is, the existence and uniqueness of solution. Further, this mathematical character is determined by the theory of characteristics. The mathematical character of the system represented by the linearized form of equation (22) is incompletely hyperbolic or hyperbolic-parabolic. It is parabolic in the $(\xi_2 - \tau)$ plane.

The rigid-wall boundary provides velocity and temperature conditions. The behavior of a real gas at ordinary conditions (Knudsen numbers less than 10^{-2}) is accurately described by the no-slip and no-temperature-jump conditions; the latter condition, corresponding to zero temperature gradient at the wall, is used. These are the only two physical conditions available. The adiabatic condition for internal energy at a solid wall is

$$\frac{\partial \iota}{\partial \xi_2} = 0 \quad (37)$$

where ι is internal energy per unit mass,

$$\iota = \frac{Q_4}{Q_1} - \sum_{i=2}^3 \frac{Q_i^2}{2Q_1^2}$$

The determination of surface density is carried out with a new governing equation formulated by combining the momentum equations to form the normal derivative of pressure,

$$\frac{\partial p}{\partial n} = (\nabla p) \cdot \left(\frac{\nabla \xi_2}{|\nabla \xi_2|} \right) + \text{contribution of viscous terms} \quad (38)$$

where n represents the direction normal to ξ_2 -surface. Since equation (38) is derived from the momentum equations, it is not a boundary condition. In the present study, the contribution of the viscous terms is neglected and $\partial p / \partial n = 0$.

At the inflow boundary and at tangent-flow open boundaries, the fluid is assumed to be inviscid. This leads to specification of boundary conditions that correspond to those for the Euler equations. These conditions are based on local one-dimensional characteristics. The local characteristics or eigenvalues determine the number and the admissible forms of boundary conditions based on one-dimensional analysis. For a hyperbolic system, the eigenvalues are real. The number of negative eigenvalues with distinct eigenvectors determines the number of boundary conditions. This number is the same as the number of inward characteristics into the computational domain. In addition, characteristic relations along a characteristic can be extrapolated along this characteristic.

Locally one-dimensional Riemann invariants are given in terms of the normal velocity components as

$$\begin{aligned} I_1 &= w_n - \frac{2a}{\gamma - 1} \\ I_2 &= w_n + \frac{2a}{\gamma - 1} \end{aligned} \quad (39)$$

where

$$w_n = \frac{(\partial \xi_2 / \partial x_1)}{[(\partial \xi_2 / \partial x_1)^2 + (\partial \xi_2 / \partial x_2)^2]^{1/2}} u - \frac{(\partial \xi_2 / \partial x_2)}{[(\partial \xi_2 / \partial x_1)^2 + (\partial \xi_2 / \partial x_2)^2]^{1/2}} v$$

The subscript n designates the direction away from the boundary. The variables u and v represent the Cartesian velocity components (nondimensionalized with respect to the free stream velocity). These equations along with conditions on the tangential velocity w_t and entropy $S = \ln(p/\rho)^\gamma$ determine Q 's. The Riemann invariants are associated with the characteristic velocities

$$\lambda_1 = w_n - a \quad \text{and} \quad \lambda_2 = w_n + a$$

When the inflow is subsonic, $w_n < 0$, and $\lambda_1 < 0$, the variables I_1 , w_t and S are all set to free stream values.

$$\begin{aligned} w_t &= \frac{(\partial \xi_2 / \partial x_2)}{[(\partial \xi_2 / \partial x_1)^2 + (\partial \xi_2 / \partial x_2)^2]^{1/2}} u_\infty - \frac{(\partial \xi_2 / \partial x_1)}{[(\partial \xi_2 / \partial x_1)^2 + (\partial \xi_2 / \partial x_2)^2]^{1/2}} v_\infty \\ S &= \gamma \end{aligned} \quad (40)$$

where γ is the ratio of specific heats. When the other characteristic velocity λ_2 is greater than 0, I_2 is extrapolated from the interior.

At the downstream (outflow) boundary, the flow is subsonic and the wake region of the airfoil is turbulent. Therefore, fluid density and momentums are extrapolated from the interior and energy is computed utilizing the value of free-stream pressure. The wake cut in a C-grid system is treated explicitly by specifying the averaged values from either side of this cut.

When it is stated, the free stream velocities and the speed of sound have been corrected for the circulation induced by the airfoil following Salas et al (ref. 11). The corrected free-stream velocities are

$$\begin{aligned} u_{c\infty} &= \cos(\alpha) + C \sin(\theta) \\ v_{c\infty} &= \sin(\alpha) - C \cos(\theta) \end{aligned} \quad (41)$$

where

$$C = \frac{C_L(1 - M_\infty^2)^{1/2}}{4\pi r[1 - M_\infty^2 \sin^2(\theta - \alpha)]}$$

with C_L and α being the lift coefficient and the angle of attack, respectively. A point on the outer boundary is fixed by the polar coordinates (r, θ) with the quarter chord location as the origin of the coordinate system. In addition, a corrected speed of sound that enforces a constant free-stream enthalpy is determined from

$$a_{c\infty}^2 = (\gamma - 1) [H_\infty - 0.5(u_{c\infty}^2 + v_{c\infty}^2)] \quad (42)$$

where

$$H_\infty = \frac{1}{(\gamma - 1)M_\infty^2} + \frac{1}{2}$$

Numerical Solution Procedure

Because we are interested in only steady-state computations, the numerical scheme given by equation (34) is modified in two ways. First, a diagonal form of this scheme developed for the Euler equations by Pulliam and Chaussee (ref. 10) is used. (Note that this diagonal form decreases the time accuracy of the numerical scheme.) Second, a spacially varying time-step is used. Both of these procedures reduce the number of iterations required for converging to a steady-state solution.

The diagonal algorithm reduces the (4×4) block pentadiagonal inversion required for solving the approximately factored form of equation (34) to (4×4) matrix multiplies and scalar pentadiagonal inversions. This algorithm cuts the operation count of the former procedure by one half, and makes it easier to vectorize the computer code. Consequently, the total computational work is decreased (refs. 10, 35).

Because the diagonal algorithm is developed only for the Euler equations, the viscous term on the left-hand side of equation (34) is neglected. The flux Jacobian matrices for the convective terms in this equation are diagonalized using real eigenvalues and a complete set of eigenvectors of each of these Jacobians (ref. 36):

$$\Lambda_{mi} = T_{mi}^{-1} \left(\frac{\partial C_{kj}}{\partial Q_k} \right) T_{ji} \quad (43)$$

where the eigenvectors of the Jacobian matrix are the columns of the matrix T_{m1} . Although the latter matrix is a function of spatial coordinates ξ_i , it is assumed not to be. With the above assumptions, the approximate factored, diagonalized algorithm of equation (34) is the following

$$\begin{aligned}
T_{m2} \left(\frac{\delta Q_m}{\delta \tau} \right)^I &= \mathfrak{R}_m^{*(n)} + D_m^{*(n)} \\
\left[I + \Delta \tau \frac{\partial}{\partial \xi_2} \Lambda_{m2} + \varrho_2 \left(\frac{1}{\mathcal{D}^{(n+1)}} \right) \right] \left(\frac{\delta Q_m}{\delta \tau} \right)^{II} &= \left(\frac{\delta Q_m}{\delta \tau} \right)^I \\
N_m \left(\frac{\delta Q_m}{\delta \tau} \right)^{III} &= \left(\frac{\delta Q_m}{\delta \tau} \right)^{II} \\
\left[I + \Delta \tau \frac{\partial}{\partial \xi_1} \Lambda_{m1} + \varrho_1 \left(\frac{1}{\mathcal{D}^{(n+1)}} \right) \right] \left(\frac{\delta Q_m}{\delta \tau} \right)^{IV} &= \left(\frac{\delta Q_m}{\delta \tau} \right)^{III} \\
T_{m1}^{-1} \left(\frac{\delta Q_m}{\delta \tau} \right)^{(n+1)} &= \left(\frac{\delta Q_m}{\delta \tau} \right)^{(IV)}
\end{aligned} \tag{44}$$

where $N_m = T_{m2}^{-1} T_{m1}$.

The above noniterative, solution algorithm consists of five one-dimensional sweeps. Each sweep requires the solution of a linear system involving either a matrix multiple or a scalar pentadiagonal system. Except for the last sweep, each sweep determines the dummy value of the time-derivative of Q_m at the $(n+1)$ time-level. The last sweep determines its true value.

The following variable time-step is used to accelerate convergence:

$$\Delta \tau = \frac{\Delta \tau_{ref}}{\sum_{i=1}^2 \left\{ |\mathcal{U}_i| + a \left[\left(\frac{\partial \xi_i}{\partial x_1} \right)^2 + \left(\frac{\partial \xi_i}{\partial x_2} \right)^2 \right]^{1/2} \right\}} \tag{45}$$

where the time-step is defined as a local function of the mesh spacing and flow-field variation. Thus, an attempt is made to use a uniform Courant number throughout the computational domain.

The finite-difference time-derivative is replaced by a finite-difference formula; for example, the following first-order formula is used in the present study:

$$\left(\frac{\delta Q_m}{\delta \tau} \right)^{(n+1)} = \frac{Q_m^{(n+1)} - Q_m^{(n)}}{\Delta \tau} \tag{46}$$

The solution of equation (46) determines Q_m :

$$Q_m^{(n+1)} = \left[Q_m^{(n)} + (\Delta \tau) \left(\frac{\delta Q_m}{\delta t} \right)^{(n+1)} \right] \tag{47}$$

To accelerate convergence to a steady state, a good initial guess on a fine grid system, say 257×57 , is first obtained. This initial guess is determined by solving the governing equations

on a 65×35 grid for a few hundred iterations, interpolating the solution, including the eddy viscosity, up to a 129×45 grid, again solving the governing equations for a few hundred iterations on this grid, and then again interpolating the solution and eddy viscosity onto the fine grid. The converged solution is then determined on this grid.

REFERENCES

1. Cebeci, T.; Clark, R. W.; Chang, K. C.; Halsey, N. D.; and Lee, K.: Airfoils with Separation and the Resulting Wakes, *Third Symposium on Numerical and Physical Aspects of Aerodynamic Flows*, California State University, Long Beach, Calif., Jan. 1985.
2. Baldwin, B. S.; and Lomax, H.: Thin-Layer Approximation and Algebraic Model for Separated Turbulent Flows, AIAA Paper 78-257, AIAA 16th Aerospace Sciences Meeting, Huntsville, Ala., Jan. 1978.
3. Beam, R.; and Warming, R. F.: An Implicit Factored Scheme for the Compressible Navier-Stokes Equations, *AIAA J.*, vol. 16, no. 4, 1978.
4. Steger, J. L.: Implicit Finite Difference Simulation of Flow about Arbitrary Two Dimensional Geometries, *AIAA J.*, vol. 16, no. 7, July 1978.
5. Cebeci, T.; and Smith, A. M. O.: A Finite-Difference Solution of the Incompressible Turbulent Boundary-Layer Equations by an Eddy-Viscosity Concept, *Proceedings Computation of Turbulent Boundary Layers - 1968 Conference*, eds. S. J. Kline, M. V. Morkovin, G. Sovaran, and D. J. Cockrell, vol. 1, Thermoscience Division, Dept. of Mech. Eng., Stanford University, Stanford, Calif., 1968.
6. Chang, K. C.; Bui, M. N.; Cebeci, T.; and Whitelaw, J. H.: The Calculation of Turbulent Wakes, Mech. Eng. Report ME-84-3, California State University, Long Beach, Calif., Sept. 1984.
7. Van Dyke, M.: *Perturbation Methods in Fluid Mechanics*, Annotated ed., Parabolic Press, 1975.
8. Mehta, U.; and Lomax, H.: Reynolds Averaged Navier-Stokes Computations of Transonic Flows - The State-of-the-Art, *Transonic Aerodynamics*, D. Nixon, ed. Progress in Astronautics and Aeronautics, vol. 81, 1982, pp. 297-375.
9. Blottner, F.: Thin-Layer Navier-Stokes Equations, *Third Symposium on Numerical and Physical Aspects of Aerodynamic Flows*, California State University, Long Beach, Calif., Jan. 1985.
10. Pulliam, T. H.; and Chaussee, D. S.: A Diagonal Form of an Implicit Approximate-Factorization Algorithm, *J. Comput. Phys.*, vol. 39, no. 2, 1981, p. 347.
11. Salas, M. D.; Jameson, A.; and Melnik, R. E.: A Comparative Study of the Nonuniqueness Problem of the Potential Equation, AIAA Paper 83-1888, AIAA 6th Computational Fluid Dynamics Conference, 1983.
12. Jameson, A.; Schmidt, W.; and Turkel, E.: Numerical Solutions of the Euler Equations by

- Finite Volume Methods Using Runge-Kutta Time-Stepping Schemes, AIAA Paper 81-1259, AIAA 14th Fluid and Plasma Dynamics Conference, Palo Alto, Calif., 1981.
13. Halsey, N. D.: Potential Flow Analysis of Multielement Airfoils Using Conformal Mapping, *AIAA J.*, vol. 17, Dec. 1979, pp. 1281-1288.
 14. Cebeci, T.; Stewartson, K.; and Williams, P. G.: Separation and Reattachment near the Leading Edge of a Thin Airfoil at Incidence, AGARD CP-291, 1981.
 15. Veldman, A. E. P.: New, Quasi-Simultaneous Method to Calculate Interacting Boundary Layers, *AIAA J.*, vol. 19, 1981, p. 79.
 16. Cebeci, T.; and Smith, A. M. O.: *Analysis of Turbulent Boundary Layers*, Academic Press, N. Y., 1974.
 17. Simpson, R. L.; Chew, Y. T.; and Shivaprasad, B. G.: The Structure of a Separating Turbulent Boundary Layer, Pt. I, Mean Flow and Reynolds Stresses, *J. Fluid Mech.*, vol. 113, 1981, p. 23.
 18. Nakayama, A.: Measurements in the Boundary Layer and Wake of Two Airfoil Models, Report. No. MDC J2403, Douglas Aircraft Co., Long Beach, Calif., 1982.
 19. Visbal, M.; and Knight, D.: Evaluation of the Baldwin-Lomax Turbulence Model for Two-Dimensional Shock-Wave Boundary Layer Interactions, AIAA Paper 83-1697, AIAA 16th Fluid and Plasma Dynamics Conference, Danvers, Mass., July 1983.
 20. York, B. J.: Evaluation of the Baldwin-Lomax Turbulence Model for a Class of Boundary Layer Flows, M. Sc. Thesis, Dept. Mech. and Aero. Eng., Rutgers - The State University, New Brunswick, N. J., Oct. 1984.
 21. Michel, R.: Etude de la Transition sur les Profils d'Aile; Etablissement d'un Critere de Determination de Point de Transition et Calcul de la Trainee de Profile Incompressible, ONERA Report. 1/1578A, 1951.
 22. Cebeci, T.; and Bradshaw, P.: *Momentum Transfer in Boundary Layers*, Hemisphere, Washington, D. C., 1977.
 23. Gregory, N.; and O'Reilly, C. L.: Low-Speed Aerodynamic Characteristics of NACA 0012 Airfoil Section, Including the Effects of Upper-Surface Roughness Simulating Hoar Frost, NPL AERO Report 1308, 1970.
 24. Loftin, Jr., L. K.; and Smith, H. A.: Aerodynamic Characteristics of 15 NACA Airfoil Sections at Seven Reynolds Numbers from 0.7×10^6 to 9.0×10^6 , NACA TN-1945, 1949.
 25. Eiseman, P.: Geometric Methods in Computational Fluid Dynamics, ICASE Report 80-11, Apr. 1980
 26. McCroskey, W. J.; McAlister, K. W.; Carr, L. W.; and Pucci, S. L.: An Experimental Study of Dynamic Stall on Advanced Airfoil Sections, Vol. 1, Summary of the Experiment, NASA TM-84245, 1982.
 27. Kaplan, C.: Effect of Compressibility at High Subsonic Velocities on the Lifting Force Acting on an Elliptic Cylinder, NACA TN-1118, 1946.

28. Agarwal, R. K.; and Deese, J. E.: Computation of Transonic Viscous Airfoil, Inlet, and Wing Flowfields, AIAA Paper 64-1551, AIAA 17th Fluid Dynamics, Plasma Dynamics, and Lasers Conference, Snowmass, Colo., 1984.
29. Noonan, K. W.; and Bingham, G. J.: Two-Dimensional Aerodynamic Characteristics of Several Rotorcraft Airfoils at Mach Numbers from 0.35 to 0.9, NASA TMX-73990, 1977.
30. Mehta, U. B.: Dynamic Stall of an Oscillating Airfoil, *Unsteady Aerodynamics*, AGARD CP 227, 1977.
31. Carr, L. W.; and Cebeci, T.: Boundary Layers on Oscillating Airfoils, *Third Symposium on Numerical and Physical Aspects of Aerodynamic Flows*, California State University, Long Beach, Calif., Jan. 1985.
32. Turkel, E.: Fast Solutions to the Steady State Compressible and Incompressible Fluid Dynamic Equations, *Lecture Notes in Physics*, Proceedings of the Ninth International Conference on Numerical Methods in Fluid Dynamics, vol. 218, Springer-Verlag, 1985.
33. Mehta, U.: Physical Aspects of Computing the Flow of a Viscous Fluid, NASA TM-85893, 1984.
34. Cebeci, T.; Chang, K. C.; Li, C.; and Whitelaw, J. H.: Turbulence Models for Wall Boundary Layers, Mech. Eng. Report ME-84-2, California State University, Long Beach, Calif., Aug. 1984. (To be published in *AIAA J.*, 1985.)
35. Pulliam T. H.; and Steger, J. L.: Recent Improvements in Efficiency, Accuracy, and Convergence for Implicit Approximate Factorization Algorithms, AIAA Paper 85-0360, AIAA 23rd Aerospace Sciences Meeting, Reno, Nev., Jan. 1985.
36. Warming, R. F.; Beam, R.; and Hyett, B. J.: Diagonalization and Simultaneous Symmetrization of the Gas-Dynamic Matrices, *Math. Comp.*, vol. 29, 1975, p. 1037.

1 Report No NASA TM-86778		2 Government Accession No		3 Recipient's Catalog No	
4 Title and Subtitle RELATIVE ADVANTAGES OF THIN-LAYER NAVIER-STOKES AND INTERACTIVE BOUNDARY-LAYER PROCEDURES				5 Report Date November 1985	
				6 Performing Organization Code	
7 Author(s) Unmeel Mehta (Ames), K. C. Chang, and Tuncer Cebeci (Douglas Aircraft Co., Long Beach, CA)				8 Performing Organization Report No A-85346	
9 Performing Organization Name and Address Ames Research Center Moffett Field, CA 94035				10 Work Unit No	
				11 Contract or Grant No	
12 Sponsoring Agency Name and Address National Aeronautics and Space Administration Washington, DC 20546				13 Type of Report and Period Covered Technical Memorandum	
				14 Sponsoring Agency Code 505-31-01	
15 Supplementary Notes Point of Contact: Unmeel Mehta, Ames Research Center, MS 202-1, Moffett Field, CA 94035, (415) 694-5548 or FTS 464-5548					
16 Abstract Numerical procedures for solving the thin-shear-layer Navier-Stokes equations and for the interaction of solutions to inviscid and boundary-layer equations are described and evaluated. To allow appraisal of the numerical and fluid dynamic abilities of the two schemes, they have been applied to one airfoil as a function of angle of attack at two slightly different Reynolds numbers. The NACA 0012 airfoil has been chosen because it allows comparison with measured lift, drag, and moment and with surface-pressure distributions. Calculations have been performed with algebraic eddy-viscosity formulations, and they include consideration of transition. The results are presented in a form that allows easy appraisal of the accuracy of both procedures and of the relative costs. The interactive procedure is computationally efficient but restrictive relative to the thin-layer Navier-Stokes procedure. The latter procedure does a better job of predicting drag than does the former. In both procedures, the location of transition is crucial for accurate or detailed computations, particularly at high angles of attack. When the upstream influence of pressure field through the shear layer is important, the thin-layer Navier-Stokes procedure has an edge over the interactive procedure.					
17 Key Words (Suggested by Author(s)) Navier-Stokes equations Interactive boundary layers Computational aerodynamics Implicit numerical methods Turbulence models				18 Distribution Statement Unlimited Subject category: 02	
19 Security Classif (of this report) Unclassified		20 Security Classif (of this page) Unclassified		21 No of Pages 51	
				22 Price* A04	

End of Document